

1 **A compressible nonhydrostatic cell-integrated semi-Lagrangian**
2 **semi-implicit solver (CSLAM-NH) with consistent and**
3 **conservative transport**

4 MAY WONG *

University of British Columbia, Vancouver, British Columbia, Canada

5 WILLIAM C. SKAMAROCK, PETER H. LAURITZEN, JOSEPH B. KLEMP

National Center for Atmospheric Research[†], Boulder, Colorado, USA

6 ROLAND B. STULL

University of British Columbia, Vancouver, British Columbia, Canada

* *Corresponding author address:* May Wong, Dept. of Earth, Ocean, and Atmospheric Sciences, University of British Columbia, 2020 - 2207 Main Mall, Vancouver, BC Canada V6T 1Z4.

E-mail: mwong@eos.ubc.ca

[†]The National Center for Atmospheric Research is sponsored by the National Science Foundation.

7 ABSTRACT

8 A cell-integrated semi-Lagrangian (CISL) semi-implicit nonhydrostatic solver (CSLAM-NH)
9 for the fully-compressible moist Euler equations in two-dimensional Cartesian (x - z) geometry
10 is presented. The semi-implicit CISL solver uses the inherently-conservative semi-Lagrangian
11 transport scheme, CSLAM, and a new flux-form semi-implicit formulation of the continuity
12 equation that ensures numerically consistent transport. The flux-form semi-implicit formu-
13 lation is based on a recent successful approach in a shallow-water equations (SWE) solver
14 (CSLAM-SW). With the new approach, the nonhydrostatic semi-implicit CISL solver is able
15 to ensure conservative and consistent transport by avoiding the need for a time-independent
16 mean reference state. Like its SWE counterpart, the nonhydrostatic solver presented here
17 is designed to be similar to typical semi-Lagrangian semi-implicit schemes, such that only
18 a single linear Helmholtz equation solution and a single call to CSLAM are required per
19 time step. To demonstrate its stability and accuracy, the solver is applied to a set of three
20 idealized test cases: a density current (dry), a gravity wave (dry), and a squall line (moist).
21 A fourth test case shows that shape preservation of passive tracers is ensured by coupling
22 the semi-implicit CISL formulation with existing shape-preserving filters. Results show that
23 CSLAM-NH solutions compare well with other existing solvers for the three test cases, and
24 that it is shape-preserving.

1. Introduction

Semi-Lagrangian semi-implicit (SLSI) schemes have been widely used in climate and numerical weather prediction (NWP) models since the pioneering work of Robert (1981) and Robert et al. (1985). The more lenient numerical stability condition in these schemes allows larger time steps and thus increased computational efficiency. Traditional semi-Lagrangian schemes are not inherently mass-conserving due to their use of grid-point interpolation, and the lack of conservation can lead to accumulation of significant solution errors (Rasch and Williamson 1990; Machenhauer and Olk 1997). To address this issue, conservative semi-Lagrangian schemes, also called cell-integrated semi-Lagrangian (CISL) transport schemes (Rancic 1992; Laprise and Plante 1995; Machenhauer and Olk 1997; Zerroukat et al. 2002; Nair and Machenhauer 2002; Lauritzen et al. 2010), have been developed. Although CISL transport schemes, when applied in fluid flow solvers, allow for locally (and thus globally) conservative transport of total fluid mass and constituent (i.e. tracer) mass, a lack of consistency arises between the numerical representation of the total dry air mass conservation, to which we will refer as the continuity equation, and constituent mass conservation equations (Jöckel et al. 2001; Zhang et al. 2008; Wong et al. 2013). Numerical consistency in the flux-form equation for a tracer requires the equation for a constant tracer field to correspond numerically to the mass continuity equation; this consistency ensures that an initially spatially uniform passive tracer field will remain so. The lack of numerical consistency between the two can lead to the unphysical generation or removal of model constituent mass, which can introduce significant errors in applications such as chemical tracer transport (Machenhauer et al. 2009).

Recently, Wong et al. (2013) introduced a new flux-form formulation of the semi-implicit CISL height conservation equation for the shallow-water equations (SWE) solver. They showed that the scheme is accurate and stable even for highly-nonlinear barotropically-unstable jets and large Courant numbers. They also found that the use of a shape-preserving filter in an inconsistent formulation of the continuity equations is ineffective, highlighting

52 the importance of numerical consistency in these models.

53 In this paper, the flux-form semi-implicit SWE formulation is extended to the fully-
54 compressible two-dimensional (x - z) moist nonhydrostatic equations for the atmosphere. We
55 refer to this new conservative and consistent nonhydrostatic solver as CSLAM-NH. A nonhy-
56 drostatic model permits fast-moving internal gravity and acoustic waves. Here, we integrate
57 the terms responsible for the acoustic waves in a semi-implicit manner to allow large time
58 steps while maintaining stability for these waves. As in Wong et al. (2013), our nonhydro-
59 static solver is based on the Conservative Semi-Lagrangian Multi-tracer transport scheme
60 (CSLAM), a CISL transport scheme developed by Lauritzen et al. (2010) that has been im-
61 plemented in NCAR’s High-Order Methods Modeling Environment [HOMME; Erath et al.
62 (2012)].

63 The semi-implicit CISL nonhydrostatic solver has six main advantages and desirable
64 properties. As we will show, our nonhydrostatic cell-integrated semi-Lagrangian solver is
65 (1) inherently mass-conserving, (2) shape-preserving, and, with the new formulation, (3) has
66 numerically consistent transport. The discretization (4) does not depend on a mean reference
67 state, but maintains the same framework as typical semi-implicit CISL solvers, where (5) a
68 single linear Helmholtz equation is solved and (6) a single application of CSLAM is needed
69 per time step.

70 The paper is organized as follows. The governing equations of the two-dimensional fully-
71 compressible nonhydrostatic system are first described in section 2. We then present the
72 proposed discretization of the governing equations, including a consistent formulation of the
73 moisture conservation equations (section 3). The desirable properties of the nonhydrostatic
74 solver are discussed in section 4. We test the nonhydrostatic solver with three idealized test
75 cases and compare results with an Eulerian split-explicit time-stepping scheme (section 5).
76 A fourth test case on numerical consistency is also presented in section 5 to demonstrate the
77 shape-preserving ability of the solver with additional passive tracers. A summary is given in
78 section 6.

2. Governing equations

The model governing equations are the two-dimensional (x - z) moist Euler equations in Cartesian geometry:

$$\frac{\partial u}{\partial t} + u \frac{\partial u}{\partial x} + w \frac{\partial u}{\partial z} = -\frac{\pi}{\rho_m} \gamma R_d \frac{\partial \Theta'_m}{\partial x} + F_u, \quad (1)$$

$$\frac{\partial w}{\partial t} + u \frac{\partial w}{\partial x} + w \frac{\partial w}{\partial z} = -\frac{\pi}{\rho_m} \gamma R_d \frac{\partial \Theta'_m}{\partial z} + \frac{g}{\rho_m} \left[\bar{\rho}_d \frac{\pi'}{\bar{\pi}} - \rho'_m \right] + F_w, \quad (2)$$

$$\frac{\partial \Theta_m}{\partial t} + \nabla \cdot (\Theta_m \mathbf{v}) = F_\Theta, \quad (3)$$

$$\frac{\partial \rho_d}{\partial t} + \nabla \cdot (\rho_d \mathbf{v}) = 0, \quad (4)$$

$$\frac{\partial Q_j}{\partial t} + \nabla \cdot (Q_j \mathbf{v}) = F_{Q_j}, \quad (5)$$

$$p = p_0 \left(\frac{R_d \Theta_m}{p_0} \right)^\gamma, \quad (6)$$

where $\pi = (p/p_0)^\kappa$ is the Exner function, $\kappa = R_d/c_p$, $\gamma = c_p/c_v = 1.4$, $R_d = 287 \text{ J kg}^{-1} \text{ K}^{-1}$, $c_p = 1003 \text{ J kg}^{-1} \text{ K}^{-1}$, and $g = 9.81 \text{ m s}^{-2}$. Perturbation variables from a time-independent hydrostatically balanced background state are used to reduce numerical errors in the calculations of the pressure gradient terms (Klemp et al. 2007). The hydrostatically balanced background state is defined as $d\bar{p}(z)/dz = -\bar{\rho}_d(z)g$. Perturbation variables are defined as $\Theta_m = \bar{\rho}_d(z)\bar{\theta}(z) + \Theta'_m$, $\pi = \bar{\pi} + \pi'$, $\rho_d = \bar{\rho}_d(z) + \rho'_d$, and the moist density $\rho_m = \rho_d(1 + q_v + q_c + q_r)$, where q_v , q_c , and q_r are the mixing ratios for water vapor, cloud, and rainwater, respectively. The $F_{(\cdot)}$ terms represent diffusion, and any diabatic effects and parameterized physics when moisture is present.

As in Klemp et al. (2007), fluxes are coupled to the dry density ρ_d . The flux variables are given as

$$\Theta_m = \rho_d \theta_m \quad \text{and} \quad Q_j = \rho_d q_j,$$

where θ_m is the modified potential temperature $\theta_m = \theta(1 + a'q_v)$ where $a' \equiv R_v/R_d \simeq 1.61$ and $q_j = (q_v, q_c, q_r)$.

The momentum equations are cast in their advective form, and all other equations, i.e., for density, potential temperature, and moist species, are cast in their conservative flux-form.

102 Pressure is a diagnostic variable given by the equation of state. The governing equations are
 103 based on Klemp et al. (2007); the pressure gradient terms in (1) and (2) have been recast in
 104 terms of Θ'_m using (6) to derive the relation

$$\nabla p = \gamma R_d \pi \nabla \Theta_m,$$

105 and enables us to form an implicit equation for Θ' (section 3). The equations are still exact
 106 and no approximations have been applied. The only difference from the governing equations
 107 in Klemp et al. (2007) is that their momentum equations are cast in the conservative flux-
 108 form, whereas the advective form is used here to facilitate the use of the traditional semi-
 109 Lagrangian method.

110 **3. A consistent and mass-conserving nonhydrostatic solver**

111 *a. CSLAM — a conservative transport scheme*

112 To ensure mass conservation, we utilize an inherently-conservative semi-Lagrangian trans-
 113 port scheme called CSLAM (Lauritzen et al. 2010). The CSLAM transport scheme is a
 114 backward-in-time CISL scheme¹, where the departure grid cell area δA^* is found by tracing
 115 the regular arrival grid cell area ΔA back in time one time-step Δt (Fig. 1a). The CSLAM
 116 discretization scheme for the lhs of (3), (4), and (5) is given by

$$\phi_{\text{exp}}^{n+1} \Delta A = \int_{\delta A^*} \phi^n dA = \phi_*^n \delta A^*$$

117 where $\phi = \Theta_m, \rho_d$, or Q_j . The superscript denotes the time level, and ϕ_{exp}^{n+1} is the explicit
 118 cell-averaged transport term computed by integrating the field ϕ^n over the departure cell
 119 area δA^* , which gives the cell-averaged departure value ϕ_*^n .

120 The departure cell area δA^* in CSLAM is found through iterative trajectory computations
 121 from the four vertices of an arrival grid cell (unfilled circles in Fig. 1b) to their departure

¹note that CSLAM may also be cast in flux-form (Harris et al. 2011)

122 points (filled circles in Fig. 1b). The departure cell area is then approximated using straight
 123 lines as cell edges² (dark grey region δA in Fig. 1b). To integrate the field ϕ^n over δA ,
 124 CSLAM implements a remapping algorithm that consists of a piecewise quasi-biparabolic
 125 subgrid-cell-reconstruction of ϕ^n in the two coordinates as in Nair and Machenhauer (2002)
 126 with an additional cross term as described in Jablonowski (2004) that helps smooth subgrid
 127 distribution near sharp gradients,

$$\phi^n(x, z) = \langle \phi^n \rangle + a^x x + b^x \left(\frac{1}{12} - x^2 \right) + a^z z + b^z \left(\frac{1}{12} - z^2 \right) + \frac{1}{2} (c^{xz} + c^{zx}) xz \quad (7)$$

128 where coefficients a^x , b^x , a^z , b^z of the reconstructed parabolic function in the two coordinates
 129 are obtained as in Nair and Machenhauer (2002), and the cross-term coefficients c^{xz} and c^{zx}
 130 are obtained as in Jablonowski (2004). An average of the two coefficients of the cross term,
 131 c^{xz} and c^{zx} , is taken to avoid a directional bias (Jablonowski 2004). The cell-average value
 132 over the Eulerian grid cell is denoted as $\langle \phi^n \rangle$.

133 The integration of the reconstruction function over the departure cell area is then com-
 134 puted. The area integration in CSLAM is transformed into a series of line integrals using the
 135 Gauss-Green theorem, and involves solving for a set of weights $w^{(i,j)}$ that depends only on the
 136 departure cell boundary. As described in Lauritzen et al. (2010), the discrete conservative
 137 transport scheme for departure cell k is

$$\int_{\delta A^*} \phi^n dA = \sum_{l=1}^{L_k} \left[\sum_{i+j \leq 2} c_l^{(i,j)} w_{kl}^{(i,j)} \right]$$

138 where $c_l^{(0,0)}$, $c_l^{(1,0)}$, $c_l^{(0,1)}$, $c_l^{(2,0)}$, $c_l^{(0,2)}$ are the coefficients for the constant, x , z , x^2 , and z^2 terms
 139 respectively, $c_l^{(1,1)}$ is the coefficient for the xz term in (7), and l is the index for the Eulerian
 140 grid cell(s) with which departure cell k overlaps (of a total of L_k overlapping Eulerian grid
 141 cells). The partitioning of the areal integration into computation of coefficients and weights
 142 greatly enhances the transport scheme's computational efficiency for multi-tracer transport,
 143 as the weights can be reused for the remapping of all tracer species in the model. For

²higher-order edge approximations have been explored in Ullrich et al. (2012)

144 full details on the basic CSLAM scheme, see Lauritzen et al. (2010); for high-resolution
 145 spherical implementations of CSLAM, the reader is referred to the modifications to the
 146 scheme documented in Erath et al. (2013). A rigorous assessment of the accuracy of linear
 147 transport using CSLAM (for the test case in Lauritzen et al. (2012)) and a comparison of
 148 CSLAM to a collection of state-of-the-art transport schemes can be found in Lauritzen et al.
 149 (2013).

150 *b. Trajectory algorithm*

151 To find the departure cell area, we trace the vertices of each arrival grid cell back one time
 152 step Δt using a trajectory algorithm described in Lauritzen et al. (2006). The trajectory is
 153 approximated and split into two segments: departure grid point to trajectory midpoint, and
 154 trajectory midpoint to arrival grid point. The split-trajectory approximation facilitates the
 155 semi-implicit formulation of the flux-form conservation equation (section 3d).

156 The displacement in the two linear segments are determined using velocities at time-level
 157 n and velocities extrapolated to time-level $n + 1$, respectively. The first segment (from the
 158 departure point position \mathbf{r}_D^n to midpoint trajectory $\mathbf{r}_{D/2}^{n+1/2}$) is approximated as

$$\mathbf{r}_{D/2}^{n+1/2} = \mathbf{r}_D^n + \frac{\Delta t}{2} \mathbf{v}_D^n, \quad (8)$$

159 We iterate (8) three times to increase the accuracy of the computation of \mathbf{v}_D^n . At each
 160 iteration, the velocities are interpolated to the estimated departure location using bicubic
 161 Lagrange interpolation. The second segment (from midpoint trajectory $\mathbf{r}_{D/2}^{n+1/2}$ to the arrival
 162 point \mathbf{r}^{n+1}) is approximated using

$$\mathbf{r}_{D/2}^{n+1/2} = \mathbf{r}^{n+1} - \frac{\Delta t}{2} \tilde{\mathbf{v}}^{n+1}, \quad (9)$$

163 where $\tilde{\mathbf{v}}^{n+1}$ is evaluated at the arrival grid point and denote velocities extrapolated to time-
 164 level $n + 1$ using a two-time-level extrapolation

$$\tilde{\mathbf{v}}^{n+1} = 2\mathbf{v}^n - \mathbf{v}^{n-1}.$$

165 To find \mathbf{r}_D^n , we take the sum of the two half-trajectories [(8) and (9)],

$$\mathbf{r}_D^n = \mathbf{r}^{n+1} - \frac{\Delta t}{2}(\mathbf{v}_D^n + \tilde{\mathbf{v}}^{n+1}).$$

166 Higher-order approximations to the trajectory can be made by including an acceleration
 167 term as described in McGregor (1993). Tests including an acceleration term (not shown)
 168 showed that such a higher-order approximation made little difference to the solutions for
 169 this suite of tests.

170 *c. Discretization of the momentum equations*

171 The momentum equations are solved using the traditional semi-Lagrangian semi-implicit
 172 method, where material derivatives such as $du/dt = \partial u/\partial t + u\partial u/\partial x + w\partial u/\partial z$ and $dw/dt =$
 173 $\partial w/\partial t + u\partial w/\partial x + w\partial w/\partial z$ (lhs of (1) and (2) respectively) are computed using a grid-point
 174 interpolation to the departure point. The two-time-level discretizations of the momentum
 175 equations are

$$\begin{aligned} u_A^{n+1} = & \left[u - \Delta t \left(\frac{1-\beta}{2} \right) \overline{\left(\frac{\pi}{\rho_m} \right)^x} \gamma R_d \delta_x \Theta' \right]_D^n + \Delta t (F_u)_D^n \\ & - \Delta t \left(\frac{1+\beta}{2} \right) \overline{\left(\frac{\pi^n}{\rho_m^n} \right)^x} \gamma R_d \delta_x \Theta_A^{n+1}, \end{aligned} \quad (10)$$

176 and

$$\begin{aligned} w_A^{n+1} = & \left[w - \Delta t \left(\frac{1-\beta}{2} \right) \overline{\left(\frac{\pi}{\rho_m} \right)^z} \gamma R_d \delta_z \Theta' \right]_D^n \\ & + \frac{\Delta t}{\rho_m^{n,z}} \left[g \bar{\rho}_d \frac{\pi'}{\bar{\pi}} - g \rho'_m \right]_{D/2}^{n+1/2z} \\ & - \Delta t \left(\frac{1+\beta}{2} \right) \overline{\left(\frac{\pi^n}{\rho_m^n} \right)^z} \gamma R_d \delta_z \Theta_A^{n+1} \\ & + \Delta t (F_w)_D^n, \end{aligned} \quad (11)$$

177 where the subscripts D , $D/2$ and A denote evaluation at the departure, midpoint trajectory,
 178 and arrival grid points respectively, and the superscripts denote the time level. The spatial

179 operators are defined as

$$\overline{(\cdot)}^x = \frac{1}{2} \left((\cdot)_{i,k} + (\cdot)_{i+1,k} \right),$$

180

$$\overline{(\cdot)}^z = \frac{1}{2} \left((\cdot)_{i,k} + (\cdot)_{i,k+1} \right),$$

181

$$\delta_x(\cdot) = \frac{(\cdot)_{i+1,k} - (\cdot)_{i,k}}{\Delta x}, \text{ and}$$

182

$$\delta_z(\cdot) = \frac{(\cdot)_{i,k+1} - (\cdot)_{i,k}}{\Delta z}.$$

183 The gradient terms responsible for the fast-moving acoustic waves are solved implicitly with
 184 the option of off-centering by setting $\beta \neq 0$. Numerical diffusion is represented in F_u and
 185 F_w in the form of second-order diffusion with physical viscosity ν ,

$$F_{(\cdot)} = \nu [\delta_x^2(\cdot) + \delta_z^2(\cdot)].$$

186 The buoyancy terms in the vertical momentum equation are solved explicitly by extrapolat-
 187 ing to time level $n + 1/2$ using

$$(\cdot)^{n+1/2} = \frac{3}{2}(\cdot)^n - \frac{1}{2}(\cdot)^{n-1},$$

188 and then interpolated to the midpoint trajectory. One way to evaluate the buoyancy term
 189 implicitly is to concurrently update the density and pressure perturbation variables (ρ'_m and
 190 π' respectively) at every iteration of $\tilde{\Theta}'_m$ in the Helmholtz solver. This implicit treatment of
 191 the buoyancy term involves updating the density perturbation using u^{n+1} and w^{n+1} guesses
 192 at that iteration, and we have yet to find a feasible way to incorporate this in the Helmholtz
 193 solver that ensures convergence at large time steps. The implicit treatment of the buoyancy
 194 terms will be the scope of future work.

195 *d. Discretization of the thermodynamic equation*

196 In our nonhydrostatic solver, we form and solve an implicit equation for Θ_m^{n+1} . The
 197 implicit equation is formed in two steps. First, we compute the explicit solution of the
 198 flux-form thermodynamic equation using the conservative transport scheme CSLAM,

$$\hat{\Theta}_m^{n+1} = \Theta_{m,\text{exp}}^{n+1} + \frac{\Delta t}{2} \left[\overline{\nabla_{\text{eul}} \cdot (\Theta_m^n \mathbf{v}^n) - \nabla_{\text{lag}} \cdot (\Theta_m^n \mathbf{v}^n)} \right] \frac{\delta A^*}{\Delta A} + \Delta t \overline{F_{\Theta_m}^n} \frac{\delta A^*}{\Delta A}, \quad (12)$$

199 where the notation $\overline{[\cdot]}$ denotes departure cell averages. The first term on the rhs of (12),
 200 $\Theta_{m,\text{exp}}^{n+1}$, is the explicit CSLAM update. The second term is a predictor-corrector term inte-
 201 grated over the departure cell to account for the discrepancy between the discrete Eulerian
 202 and Lagrangian flux divergences in the semi-implicit flux-form correction term. Similarly,
 203 in F_{Θ_m} , second-order diffusion (with mixing coefficient given by ν times the Prandtl num-
 204 ber) and the diabatic tendency from the microphysical scheme are evaluated explicitly and
 205 integrated over the departure cell area. Since the predictor-corrector and the forcing terms
 206 depend only on values at the previous time level, they can be evaluated along with $\Theta_{m,\text{exp}}^{n+1}$
 207 in a single call to CSLAM, giving $\hat{\Theta}_m^{n+1}$. Then, to allow for coupling to the momentum
 208 equations, a semi-implicit flux-form correction term is used to form the implicit equation

$$\tilde{\Theta}_m^{n+1} = \hat{\Theta}_m^{n+1} - \frac{\Delta t}{2} \left[\overline{\nabla_{\text{eul}} \cdot (\hat{\Theta}_m^{n+1} \mathbf{v}^{n+1}) - \nabla_{\text{lag}} \cdot (\hat{\Theta}_m^{n+1} \tilde{\mathbf{v}}^{n+1})} \right], \quad (13)$$

209 where $\tilde{\Theta}_m^{n+1}$ is the value of Θ_m at the new time level except for a final saturation adjustment
 210 that takes place at the end of the time step to correct the diabatic tendency using the
 211 microphysics scheme. The new tendency is then carried over to the next time step to be
 212 used as an estimate of the diabatic term in (12).

213 The form of the semi-implicit correction term (square-bracketed terms in (13)) stems from
 214 the split-divergence approximation used in the trajectory computation. The semi-implicit
 215 discretization for Θ_m^{n+1} is based on the flux-form scheme presented in Wong et al. (2013) for
 216 the height equation in their shallow-water equations solver. The flux-form scheme is based

217 on the derivation of a similar semi-implicit discretization for the shallow-water model found
 218 in Lauritzen et al. (2006), but the latter scheme uses a time-independent reference state,
 219 with which it becomes difficult to ensure numerical consistency and maintain conservative
 220 properties (discussed in section 4). Instead of using a time-independent reference state, we
 221 form the semi-implicit correction term using the explicit solution $\hat{\Theta}_m^{n+1}$ from (12).

222 The semi-implicit correction term is defined as the difference between an Eulerian flux
 223 divergence and a Lagrangian flux divergence. On an Arakawa C-grid, these would be defined
 224 as

$$\begin{aligned} \nabla_{\text{eul}} \cdot (\Theta_m \mathbf{v}) &= \frac{1}{\Delta x} \left[(\overline{\Theta}_m^x u)_r - (\overline{\Theta}_m^x u)_l \right] \\ &\quad + \frac{1}{\Delta z} \left[(\overline{\Theta}_m^z w)_t - (\overline{\Theta}_m^z w)_b \right], \end{aligned} \quad (14)$$

225 and

$$\begin{aligned} \nabla_{\text{lag}} \cdot (\Theta_m \mathbf{v}) &= \frac{1}{\Delta x \Delta z} \left[\overline{\Theta}_m^x \mathcal{F}_r - \overline{\Theta}_m^x \mathcal{F}_l \right. \\ &\quad \left. + \overline{\Theta}_m^z \mathcal{F}_t - \overline{\Theta}_m^z \mathcal{F}_b \right], \end{aligned} \quad (15)$$

226 respectively, and $\mathcal{F}_{(\cdot)}$ are Lagrangian flux areas, where the subscripts r, l, t, b denote the
 227 right, left, top, and bottom cell faces of an Eulerian grid cell (Fig. 2). We use an exact
 228 computation of the Lagrangian flux divergence in an Eulerian manner, where Lagrangian
 229 flux areas $\mathcal{F}_{(\cdot)}$ through each cell face are defined as

$$\mathcal{F}_r = \overline{u}_r^{zz} \Delta z - (u_{c2} w_{c3} - u_{c3} w_{c2}) \Delta t / 2,$$

230

$$\mathcal{F}_l = \overline{u}_l^{zz} \Delta z - (u_{c1} w_{c4} - u_{c4} w_{c1}) \Delta t / 2,$$

231

$$\mathcal{F}_t = \overline{w}_t^{xx} \Delta x - (u_{c3} w_{c4} - u_{c4} w_{c3}) \Delta t / 2,$$

232

$$\mathcal{F}_b = \overline{w}_b^{xx} \Delta x - (u_{c2} w_{c1} - u_{c1} w_{c2}) \Delta t / 2,$$

233 where the spatial operators are defined as

$$\overline{(\cdot)}^{xx} = \frac{1}{4} \left((\cdot)_{i-1,k} + 2(\cdot)_{i,k} + (\cdot)_{i+1,k} \right),$$

234

$$\overline{(\cdot)}^{zz} = \frac{1}{4} \left((\cdot)_{i,k-1} + 2(\cdot)_{i,k} + (\cdot)_{i,k+1} \right).$$

235 The terms proportional to $\Delta t/2$ correct for the geometric differences between the Eulerian
 236 and Lagrangian flux divergences (shaded areas in Fig. 2). (For full details on the derivation
 237 of \mathcal{F} and $\nabla_{\text{lag}} \cdot (\Theta_m \mathbf{v})$, see Wong et al. (2013)).

238 Using (14) and (15), the explicit equation for $\hat{\Theta}_m^{n+1}$ (12) and implicit equation for $\tilde{\Theta}_m^{n+1}$
 239 (13) can be rewritten as

$$\hat{\Theta}_m^{n+1} = \Theta_{m,\text{exp}}^{n+1} + \frac{\Delta t}{2} \left[\overline{\nabla_{\text{eul}} \cdot (\Theta_m^n \mathbf{v}'^n)} \right] \frac{\delta A^*}{\Delta A} + \Delta t \left[\overline{F_{\Theta_m}^n} \right] \frac{\delta A^*}{\Delta A}, \quad (16)$$

240 and

$$\tilde{\Theta}_m^{n+1} = \hat{\Theta}_m^{n+1} - \frac{\Delta t}{2} \left[\overline{\nabla_{\text{eul}} \cdot (\hat{\Theta}_m^{n+1} \mathbf{v}'^{n+1})} \right], \quad (17)$$

241 respectively, where \mathbf{v}' is a corrective velocity and

$$\begin{aligned} \nabla_{\text{eul}} \cdot (\Theta_m \mathbf{v}') &= \frac{1}{\Delta x} \left[\overline{\Theta_m^x (u_r - \mathcal{F}_r / \Delta z)} - \overline{\Theta_m^x (u_l - \mathcal{F}_l / \Delta z)} \right] \\ &\quad + \frac{1}{\Delta z} \left[\overline{\Theta_m^z (w_t - \mathcal{F}_t / \Delta x)} - \overline{\Theta_m^z (w_b - \mathcal{F}_b / \Delta x)} \right]. \end{aligned}$$

242 *e. Helmholtz equation*

243 The Helmholtz equation with variable coefficients for the semi-implicit problem is solved
 244 using a conjugate-residual solver. Substitution of the momentum equations (10) and (11)
 245 into (17) forms the Helmholtz equation for $\tilde{\Theta}_m^{n+1}$,

$$\begin{aligned} & - \left(\frac{\Delta t}{2} \right)^2 \gamma R_d (1 + \beta) \left[\overline{\delta_x \left(\hat{\Theta}_m^{n+1} \frac{\pi^n}{\rho_m^n} \delta_x \tilde{\Theta}_m^{n+1} \right)} \right. \\ & \quad \left. + \overline{\delta_z \left(\hat{\Theta}_m^{n+1} \frac{\pi^n}{\rho_m^n} \delta_z \tilde{\Theta}_m^{n+1} \right)} \right] + \tilde{\Theta}_m^{n+1} \\ & = R_\Theta - \frac{\Delta t}{2} (1 + \beta) \left[\overline{\delta_x \left(\hat{\Theta}_m^{n+1} R_u \right)} + \overline{\delta_z \left(\hat{\Theta}_m^{n+1} R_w \right)} \right]. \end{aligned} \quad (18)$$

246 The terms R_u , R_w , and R_Θ represent the known terms in (10), (11), and (17). The explicit
 247 solution $\hat{\Theta}_m^{n+1}$ from CSLAM is computed prior to solving (18).

248 Using the explicit solution $\hat{\Theta}_m^{n+1}$ allows for a straightforward and consistent formulation
 249 between the thermodynamic and continuity equations, as long as the reconstruction of Θ_m is
 250 performed in a consistent manner. To ensure this, in CSLAM we follow Nair and Lauritzen
 251 (2010) in separating the sub-grid-cell reconstructions for ρ_d and θ_m , and compute the second-
 252 order reconstruction function $\Theta_m(x, z)$ as

$$\Theta_m(x, z) = \langle \rho_d \rangle \theta_m(x, z) + \langle \theta_m \rangle \left(\rho_d(x, z) - \langle \rho_d \rangle \right), \quad (19)$$

253 where $\langle \rho_d \rangle$ and $\langle \theta_m \rangle$ are Eulerian grid cell values, and $\rho_d(x, z)$ and $\theta_m(x, z)$ are reconstruction
 254 functions. To check for consistency, we substitute a field of constant θ_m , i.e. $\theta_m(x, z) =$
 255 $\langle \theta_m \rangle = 1$, in (19) and see that the rhs of (19) properly reduces to $\rho_d(x, z)$.

256 In summary, the solution procedure for obtaining solutions for $\tilde{\Theta}_m^{n+1}$, u^{n+1} , and w^{n+1} , is
 257 as follows: (i) obtain solution for $\tilde{\Theta}_m^{n+1}$ by solving the Helmholtz equation (18), (ii) substitute
 258 solution for $\tilde{\Theta}_m^{n+1}$ into (10) and (11) to obtain solutions for u^{n+1} and w^{n+1} respectively, and
 259 (iii) recalculate $\tilde{\Theta}_m^{n+1}$ using u^{n+1} and w^{n+1} to eliminate any roundoff errors. This solution
 260 procedure is similar to that used in Wong et al. (2013) for the shallow-water equations.

261 *f. Discretization of the continuity equation*

262 We ensure that the flux-form thermodynamic equation is consistent with the continuity
 263 equation by using the same numerical scheme, with the inclusion of the semi-implicit cor-
 264 rection terms in the continuity equation. Again, we first use CSLAM to obtain the explicit
 265 solution $\hat{\rho}_d^{n+1}$ in a similar manner as in (16),

$$\hat{\rho}_d^{n+1} = \rho_{d,\text{exp}}^{n+1} + \frac{\Delta t}{2} \left[\overline{\nabla_{\text{eul}} \cdot (\rho_d^n \mathbf{v}^n)} \right] \frac{\delta A^*}{\Delta A}. \quad (20)$$

266 Then, we add the semi-implicit correction term to (20) to be consistent with (17),

$$\rho_d^{n+1} = \hat{\rho}_d^{n+1} - \frac{\Delta t}{2} \left[\nabla_{\text{eul}} \cdot (\hat{\rho}_d^{n+1} \mathbf{v}^{n+1}) \right]. \quad (21)$$

267 The new time-level correction term is evaluated by back-substituting the solution of the
 268 velocity field \mathbf{v}^{n+1} into \mathbf{v}^{m+1} .

269 *g. Discretization of moisture conservation equations*

270 The flux variables of mixing ratios of water vapor q_v , cloud water q_c , and rainwater q_r
 271 are included as prognostic variables in the nonhydrostatic solver. Moist mass conservation
 272 equations are integrated using CSLAM. To ensure moisture conservation, numerical consis-
 273 tency between the continuity equation and the moisture conservation equations needs to be
 274 ensured. Numerical inconsistency between the continuity equation and other scalar conser-
 275 vation equations can lead to spurious generation or removal of scalar mass, despite using
 276 inherently mass-conserving advection schemes.

277 A consistent formulation of the moisture conservation equations using the scheme in
 278 Wong et al. (2013) for the flux variables $Q_j = \rho_d q_j$ where $q_j = (q_v, q_c, q_r)$ is

$$\hat{Q}_j^{n+1} = Q_{j,\text{exp}}^{n+1} + \frac{\Delta t}{2} \left[\overline{\nabla_{\text{eul}} \cdot (Q_j^n \mathbf{v}^m)} \right] \frac{\delta A^*}{\Delta A} + \Delta t \left[\overline{F_{q_j}^n} \right] \frac{\delta A^*}{\Delta A}, \quad (22)$$

$$\tilde{Q}_j^{n+1} = \hat{Q}_j^{n+1} - \frac{\Delta t}{2} \left[\nabla_{\text{eul}} \cdot (\hat{Q}_j^{n+1} \mathbf{v}^{m+1}) \right] \quad (23)$$

281 where \mathbf{v}^m , \mathbf{v}^{m+1} and the computations for $\nabla_{\text{eul}} \cdot (\cdot)$ are the same as in (21). The explicit
 282 CSLAM solution \hat{Q}_j^{n+1} [(22)] is computed using a consistent reconstruction as in (19). F_{q_j}
 283 represents second-order diffusion with a mixing coefficient same as that for Θ_m , and any
 284 diabatic tendencies from the microphysics.

285 *h. Diabatic processes*

286 Microphysical processes are modelled using the simple warm-rain Kessler parameteriza-
 287 tion, as described in Klemp and Wilhelmson (1978). In the evaluation of the thermodynamic
 288 and moisture conservation equations, the diabatic forcing is approximated in F_{Θ_m} and F_{Q_j}

289 [(16) and (22), respectively] using the most up-to-date values integrated over the depar-
 290 ture cell. These values are then removed from the solutions prior to calling the Kessler
 291 microphysics scheme. The included microphysical processes are (1) condensation of water
 292 vapor into cloud-water, (2) autoconversion by diffusion and collection of cloud-water into
 293 rain-water, (3) evaporation of cloud-water and rain, and (4) precipitation of rain which is
 294 removed when it reaches the surface. These microphysical processes are computed as a final
 295 adjustment at the end of the time step, advancing $\tilde{\Theta}_m^{n+1}$ and \tilde{Q}_j^{n+1} to Θ_m^{n+1} and Q_j^{n+1} in a
 296 manner that is consistent with saturation conditions at the new time level.

297 *i. Diagnostic equation of state*

298 Pressure is a diagnostic variable computed using the equation of state (6),

$$p = p_0 \left(\frac{R_d \Theta_m}{p_0} \right)^\gamma$$

299 where p_0 is the reference surface pressure set to 100 kPa.

300 *j. Consistency and shape-preservation*

301 In the CSLAM reconstruction step, we reconstruct Q_j using (19) described in section 3e
 302 to ensure consistency. To ensure shape preservation, we follow the two steps as described in
 303 Wong et al. (2013). First, we use the simple 2D filter by Barth and Jespersen (1989) that
 304 searches for new local minima and maxima in the reconstruction function of a scalar field
 305 such as moisture mixing ratio q_j , and scales the function if these values exceed those in the
 306 neighbouring cell. For chemistry applications, preservation of linear correlations in tracers
 307 is important, and it has been found that the limiter preserves linear correlations between
 308 tracers, whereas typically linear correlation is only preserved when the limiter is not applied.
 309 Second, to ensure shape-preservation in the flux-divergence terms, we compute the upwind
 310 moist species mixing ratio q_j^* by first decoupling Q_j from ρ_d . Then, the flux divergences are

311 computed by centering density to each of the cell faces, i.e.

$$\begin{aligned} \nabla_{\text{eul}} \cdot \rho_d q_j \mathbf{v}' &= \frac{1}{\Delta x} \left[(\bar{\rho}_d^x q_j^* u')_r - (\bar{\rho}_d^x q_j^* u')_l \right] \\ &\quad + \frac{1}{\Delta z} \left[(\bar{\rho}_d^z q_j^* w')_t - (\bar{\rho}_d^z q_j^* w')_b \right]. \end{aligned}$$

312 The upwind q_j^* values are determined using \mathbf{v}' .

313 4. Desirable properties of CSLAM-NH

314 The flux-form nonhydrostatic semi-implicit CISK solver CSLAM-NH has six main ad-
 315 vantages and desirable properties: (i) inherently mass-conserving using the conservative
 316 semi-Lagrangian transport scheme CSLAM, (ii) ensures numerically consistent transport,
 317 (iii) independent of a mean reference state, (iv) shape-preserving, and (v) like typical semi-
 318 implicit solvers, CSLAM-NH requires solving a single linear Helmholtz equation and (vi) a
 319 single application of CSLAM at each time step.

320 CSLAM-NH uses a formulation of the discretized continuity equation that ensures nu-
 321 merical consistency for a cell-integrated semi-Lagrangian (CISK) solver. In CSLAM-NH, a
 322 Helmholtz equation for the potential temperature perturbation is solved. Traditionally, to
 323 avoid solving a nonlinear Helmholtz equation, the flux divergence term that is coupled to
 324 the momentum equations is often first linearized around a mean reference state $\Theta_{m,\text{ref}}$, e.g.

$$\begin{aligned} \Theta_m^{n+1} &= \Theta_{m,\text{exp}}^{n+1} - \frac{\Delta t}{2} \left[\nabla_{\text{eul}} \cdot (\Theta_{m,\text{ref}} \mathbf{v}^{m+1}) \right] \\ &\quad + \frac{\Delta t}{2} \overline{\left[\nabla_{\text{eul}} \cdot (\Theta_{m,\text{ref}} \mathbf{v}^m) \right]} \frac{\delta A^*}{\Delta A} \\ &\quad + \Delta t \overline{\left[F_{\Theta_m}^n \right]} \frac{\delta A^*}{\Delta A}, \end{aligned} \tag{24}$$

325 where $\Theta_{m,\text{ref}}$ is a mean reference state that is often time-independent and varies with height.
 326 A choice of reference state can be the hydrostatic background state $\bar{\rho}_d \bar{\theta}$. The scheme (24) is
 327 a nonhydrostatic extension to the SWE semi-implicit CISK continuity equation in Lauritzen
 328 et al. (2006).

329 To ensure conservation of potential temperature, it is important for the discrete ther-
 330 modynamic equation to be numerically consistent with the discrete continuity equation. A
 331 discretized continuity equation numerically consistent with (24) is

$$\begin{aligned} \rho_d^{n+1} = \rho_{d,\text{exp}}^{n+1} - \frac{\Delta t}{2} \left[\nabla_{\text{eul}} \cdot (\rho_{d,\text{ref}} \mathbf{v}^{n+1}) \right] \\ + \frac{\Delta t}{2} \overline{\left[\nabla_{\text{eul}} \cdot (\rho_{d,\text{ref}} \mathbf{v}^n) \right]} \frac{\delta A^*}{\Delta A}. \end{aligned} \quad (25)$$

332 Transported material, such as moisture and passive tracers with some mixing ratio q , are
 333 often solved explicitly using the CISL transport scheme, i.e.,

$$\phi^{n+1} = \phi_{\text{exp}}^{n+1} + \Delta t \overline{\left[F_{\phi}^n \right]} \frac{\delta A^*}{\Delta A}, \quad (26)$$

334 where $\phi = \rho_d q$ is the scalar mass and $\overline{\left[F_{\phi}^n \right]}$ represents diffusion and any diabatic tendency
 335 evaluated at time level n over the departure cell. Such explicit schemes would lead to
 336 numerical inconsistency between the discrete CISL continuity equation (25) and the discrete
 337 constituent mass conservation equations such as (26). If the discrete conservation equation
 338 is consistent with the discrete continuity equation, the former should reduce to the latter
 339 when q is a constant, and an initially spatially uniform passive tracer field should remain so.
 340 The inconsistent flux-divergence correction term in (25) can spuriously generate or remove
 341 moisture or tracer mass in the model.

342 Alternatively, one can formulate the discrete scalar conservation equation in a manner
 343 consistent with (25) by including the flux-divergence correction terms,

$$\begin{aligned} \phi^{n+1} = \phi_{\text{exp}}^{n+1} - \frac{\Delta t}{2} \left[\nabla_{\text{eul}} \cdot (\phi_{\text{ref}} \mathbf{v}^{n+1}) \right] \\ + \frac{\Delta t}{2} \overline{\left[\nabla_{\text{eul}} \cdot (\phi_{\text{ref}} \mathbf{v}^n) \right]} \frac{\delta A^*}{\Delta A} \\ + \Delta t \overline{\left[F_{\phi}^n \right]} \frac{\delta A^*}{\Delta A}. \end{aligned} \quad (27)$$

344 However, determining an appropriate choice for reference state ϕ_{ref} is difficult, making a
 345 numerically consistent formulation such as (27) hard to implement.

346 The formulations we present for the thermodynamic, density, and moisture conservation
 347 equations [(17), (21), and (23), respectively] are all numerically consistent with one another.

348 These consistent formulations are made possible by avoiding the use of a mean reference
349 state. In our formulation, we use the explicit CSLAM solution instead of a mean reference
350 state in the flux-divergence correction terms. This approach eliminates the difficult choice
351 of a mean reference state ϕ_{ref} for moisture or tracer mass.

352 Even if an appropriate choice of ϕ_{ref} can be found, using a time-independent mean
353 reference state in (27) can be problematic for regions with little moisture or tracer mass
354 ($\hat{\phi}^{n+1} \ll 1$). Depending on the magnitude of ϕ_{ref} , the flux divergences are likely nonzero for
355 a divergent flow and can, therefore, generate or remove unphysical mass (Lauritzen et al.
356 2008). In the nonhydrostatic solver presented here, by computing the flux divergences of
357 the explicit solution $\hat{\phi}^{n+1}$, the magnitude of the flux divergences are better approximated
358 for regions with little moisture or tracer mass.

359 As scalar mass conservation is not guaranteed in an inconsistent solver, these solvers
360 also generally do not preserve the shape of scalar fields such as mixing ratios, even when
361 shape-preserving filters are applied to the transport scheme. The implications are that the
362 scalar field may no longer be positive-definite, and new unphysical minima and maxima can
363 occur due to under- and overshooting, respectively. The consistent and shape-preserving
364 transport in the proposed solver ensures that no new (unphysical) minimum and maximum
365 (within machine roundoff) will occur.

366 5. Idealized test cases

367 Two of the three idealized test cases presented, namely a density current simulation and
368 a gravity wave simulation, are commonly used as benchmarks for testing nonhydrostatic
369 solvers. The third idealized test case is a 2D squall line simulation, where the stability of the
370 model is tested with latent heating modeled by a simple warm-rain microphysics scheme.
371 In addition to comparing with available solutions in the literature, comparisons with an
372 Eulerian split-explicit model with 2nd-order advection are also presented.

373 *a. Density current*

374 The nonlinear density current test case, described in Straka et al. (1992), is widely used
 375 as a benchmark test for nonhydrostatic solvers (e.g. Klemp et al. 2007; Xue et al. 2000).
 376 An initial cold temperature perturbation is centered in the domain, and the negatively
 377 buoyant cold air descends to the surface and forms symmetric density currents propagating
 378 in opposite directions. Straka et al. (1992) provides a well-documented comparison among
 379 various compressible and quasi-compressible solvers as well as a high-resolution benchmark
 380 solution.

381 The numerical domain is centered at $x = 0.0$ km, with $-25.6 \text{ km} \leq x \leq 25.6 \text{ km}$ and
 382 $0 \leq z \leq 6.4 \text{ km}$. As described in Straka et al. (1992), the initial condition is given by a
 383 temperature perturbation ΔT , where

$$\Delta T = \begin{cases} 0.0^\circ\text{C} & \text{if } L \geq 1.0 \\ -15.0^\circ\text{C} [\cos(\pi L) + 1.0] / 2 & \text{if } L < 1.0, \end{cases}$$

384 where $L = \sqrt{[(x - x_c)/x_r]^2 + [(z - z_c)/z_r]^2}$ where $(x_c, z_c) = (0.0, 3.0)$ km is the center of
 385 the perturbation, and its width and depth are given by $x_r = 4.0$ km and $z_r = 2.0$ km. The
 386 surface temperature θ_0 is at 300 K in a horizontally homogeneous and neutral environment.
 387 A constant physical viscosity of $75 \text{ m}^2 \text{ s}^{-1}$ is used. The domain is an x -periodic channel with
 388 reflective boundary conditions along the upper and lower boundaries as specified by Straka
 389 et al. (1992) that require $\partial u / \partial z = w = \partial \rho / \partial z = \partial \Theta / \partial z = 0$.

390 Following Straka et al. (1992), we simulate the density current test case using grid spac-
 391 ings $\Delta x = \Delta z = 400, 200, 100, 50, 25$ m, with Eulerian time step sizes of $\Delta t = 4, 2, 1, 0.5$, and 0.25
 392 s, respectively. Figure 3 shows the potential temperature perturbation (θ') from its mean
 393 state from CSLAM-NH and the Eulerian split-explicit scheme with 2nd-order advection at
 394 the simulation end time of 15 min using different model resolutions.

395 The density current is clearly under-resolved using a 400 m-grid spacing, with only the
 396 main rotor marginally resolved ($7 \text{ km} \leq x \leq 9 \text{ km}$). A grid-spacing of 200 m gives a better

397 resolution of the main rotor as well as a second rotor ($11 \text{ km} \leq x \leq 12 \text{ km}$); however the
398 leading third rotor is still under-resolved. For resolutions finer than $\Delta x = \Delta z = 100 \text{ m}$,
399 all three rotors are well-resolved with the solutions converging and indistinguishable by eye
400 between 50 m and 25 m grid spacings. The differences among the model resolutions agree
401 well with those documented in other nonhydrostatic solvers such as in Straka et al. (1992),
402 Xue et al. (2000), Skamarock and Klemp (2008), and Melvin et al. (2010).

403 Positions of the density current front (specified to be at $\theta' = -1 \text{ K}$), the minimum and
404 maximum θ' values in the domain, and $\sum \theta'_{\text{sampled}}$ for all θ'_{sampled} and $\theta'_{\text{sampled}} > 0$, and
405 $\sum \theta'^2_{\text{sampled}}$ are shown in Table 1. We also compare the results with those using SLICE (Table
406 II of Melvin et al. (2010)) and REFC25, the 25 m reference solution in Table IV of Straka
407 et al. (1992). In computing the summation statistics, θ'_{sampled} from each of the CSLAM-
408 NH runs (except for the 400 m grid-spacing run) are sampled at 200 m resolution. This
409 sampling is done so that we can make a direct comparison with the statistics of REFC25
410 in Straka et al. (1992) (where they sampled REFC25 at 200 m resolution). Statistics from
411 the 25 m solution agree closely with the nonhydrostatic SLICE model, with a similar slight
412 discrepancy in the density front location when compared to REFC25. Both CSLAM-NH and
413 SLICE are semi-Lagrangian models with inherent dissipation and order of accuracy different
414 from REFC25, an Eulerian compressible solver with 2nd-order advection; these differences
415 could lead to the slight discrepancy in the density front locations. In addition to model
416 differences, like the SLICE model, a different time step size is used to compute the 25 m
417 solution (16 times larger than that used to compute REFC25). At coarser resolutions (400
418 m and 200 m), the minimum θ' values are colder than those in SLICE; the front locations
419 therefore also travelled farther out from the centerline. Analytically, the maximum θ' should
420 remain zero throughout the simulation, as is the case in the higher resolution runs (50 m and
421 25 m). The contribution of positive θ' values in $\sum \theta'_{\text{sampled}}$ is also small at these resolutions
422 (in the order of $1 \times 10^{-5} \text{ K}$ and $1 \times 10^{-8} \text{ K}$ respectively), increasing up to the order of 1×10^{-1}
423 K at 200 m. (Straka et al. (1992) only reported values up to 4 decimal points.)

424 For the next simulation, mean background wind of $\bar{U} = 20 \text{ m s}^{-1}$ is applied to the
425 described test case, as is done in Skamarock and Klemp (2008) to examine phase errors.
426 Solutions from CSLAM-NH and the Eulerian split-explicit 2nd-order advection scheme of
427 both the left- and right-moving currents at time 15 min using $\Delta x = \Delta z = 200, 100,$ and
428 50 m are shown in Fig. 4. Time step sizes are the same as in Fig. 3. The solutions from
429 CSLAM-NH in general show proper symmetry about the translating centerline, although
430 very subtle differences between the secondary rotors in the left- and right-moving currents
431 are noticeable at 200 m and 100 m grid spacing. As a comparison, the Eulerian split-explicit
432 2nd-order advection scheme shows noticeably larger errors in the right-moving current as
433 expected due to the right-moving current moving at a greater speed than the other (causing
434 larger advective phase errors).

435 For this test case, we found that the maximum stable time step size in CSLAM-NH is
436 double of that of the Eulerian scheme. Fig. 5 shows solutions for tests where $\bar{U} = 0 \text{ m}$
437 s^{-1} at $\Delta x = \Delta z = 100 \text{ m}$ using a time step size of 3 s and 4 s, whereas the maximum
438 stable Eulerian time step size is $\Delta t = 2 \text{ s}$. The solution using a large time step of 4 s is
439 almost indistinguishable by eye from the 25 m high-resolution solutions (Fig. 3). With
440 mean advection ($\bar{U} = 20 \text{ m s}^{-1}$), the maximum stable time step in CSLAM-NH is 3 s. As we
441 increase the time step size to 4 s, the phase error was large enough to form unphysically steep
442 gradients at the leading edge of the right-moving current, which then caused the violation
443 of the Lipschitz stability condition. The maximum stable time step in the Eulerian model
444 is 1.5 s. Using a time step size of 5 s, instability was observed in the vicinity of the leading
445 edge of the subsiding cold air for both cases with and without the mean wind.

446 *b. Gravity wave*

447 A second test case of a gravity wave in a periodic channel with solid, free-slip upper-
448 and lower-boundary conditions is used to evaluate the nonhydrostatic solver. The test case
449 is described in Skamarock and Klemp (1994), where they presented results for a Boussinesq

450 atmosphere. The test case is characterized by an initial potential temperature perturbation
 451 of amplitude $\Delta\theta_0$,

$$\theta(x, z, t = 0) = \Delta\theta_0 \frac{\sin(\pi z/H)}{1 + (x - x_c)^2/a^2}.$$

452 where $\Delta\theta_0 = 10^{-2}$ K, $a = 5$ km is the half-width of the initial perturbation, $H = 10$ km
 453 is the total depth of the domain, and $x_c = 0.25L$, where $L = 300$ km is the length of the
 454 domain. The background atmospheric stratification has a constant Brunt-Väisälä frequency
 455 $N = 10^{-2}$ s $^{-1}$. For one simulation, no mean wind ($\bar{U} = 0$) is prescribed. The other simulation
 456 uses a mean wind of $\bar{U} = 20$ m s $^{-1}$, advecting the solution to the right while the two gravity
 457 wave modes propagate in opposite directions. Again, the mean advection of the solution
 458 accentuates any advective phase speed errors in the scheme. The boundary condition is
 459 implemented by linear extrapolating u , Θ , and ρ values into the boundary, consistent with
 460 the free-slip boundary conditions, and setting $w = 0$.

461 We run the gravity wave test case at grid spacings $\Delta x = \Delta z = 1$ km, 500 m, and
 462 250 m using Eulerian time step sizes $\Delta t = 12$ s, 6 s, and 3 s, respectively. Solutions from
 463 CSLAM-NH at the three resolutions for $\bar{U} = 0$ (not shown) are indistinguishable by eye
 464 from the 250 m and 500 m solutions for $\bar{U} = 20$ m s $^{-1}$ in Fig. 6 and compare well with
 465 those using the WRF-ARW model (solutions using the 5th- and 6th-order advection scheme
 466 are available at http://www.mmm.ucar.edu/projects/srnwp_tests/IG_waves/ig_wave.html),
 467 with the 2nd-order advection scheme of the same Eulerian split-explicit scheme (not
 468 shown), and with the SLICE nonhydrostatic vertical model in Melvin et al. (2010). In
 469 Skamarock and Klemp (1994), the solution presented for this nonhydrostatic test case uses
 470 a Boussinesq model, where the symmetry of the analytic Boussinesq solution in both x
 471 and z is maintained. The density variation in the full Euler equations results in solutions
 472 that are asymmetric in z , as observed in the CSLAM-NH solutions, the 2nd-order Eulerian
 473 solutions, the 5th-order Eulerian solutions, as well as the SLICE nonhydrostatic vertical
 474 model solutions.

475 Like in the density current test, we impose a mean advection wind $\bar{U} = 20$ m s $^{-1}$ to

476 examine phase errors. These tests are made at the same grid spacings and time step sizes
477 as in the no mean wind case. The right- and left-moving waves from CSLAM-NH exhibit
478 nearly perfect symmetry, indicating there is minimal phase error in the solutions. The
479 Eulerian split-explicit 2nd-order advection scheme shows more noticeable phase errors (Fig.
480 6).

481 Testing of CSLAM-NH using larger time steps in this gravity wave test case reveals a
482 numerical stability condition that is sensitive to the stratification N . (We note that CSLAM-
483 NH is unconditionally stable for $N = 0$, i.e. for a near-pure advection case of the initial
484 warm perturbation.) We evaluate the maximum stable CSLAM-NH time step size for the
485 gravity wave case with a mean advection wind speed of $\bar{U} = 20 \text{ m s}^{-1}$ ($\Delta x = \Delta z = 1$
486 km) over a range of N (0.01, 0.015, and 0.02 s^{-1}). Since the gravity wave phase speed
487 varies with N , we increase/decrease the simulation time length as appropriate such that the
488 gravity wave solutions are similar to those shown in Fig. 6; for example, for $N = 0.015$
489 s^{-1} , the simulation time is reduced to 2000 s. Test results showed that the maximum stable
490 CSLAM-NH time step sizes are $\Delta t_{\text{max}} = 38, 35,$ and 32 s for $N = 0.01, 0.015,$ and 0.02 s^{-1} ,
491 respectively, whereas in the case of the Eulerian split-explicit scheme, the maximum stable
492 large time steps are found to be $\Delta t = 60, 55,$ and 50 s (with small time step size of 2.4 s),
493 respectively, limited by the stability condition of the advection scheme. The buoyancy terms
494 in the vertical momentum equation are integrated explicitly in CSLAM-NH, and handled
495 implicitly in the Eulerian scheme. When we remove the buoyancy terms from the implicit
496 step and solve them explicitly in the Eulerian model, the time step sizes required to obtain
497 solutions of similar accuracy as those from the vertically implicit model are reduced by 20–
498 35%, and are closer to those found in CSLAM-NH. The devising of an integration scheme
499 that handles the buoyancy terms implicitly in CSLAM-NH will require a robust and stable
500 way of updating the density perturbation in the Helmholtz solver, and this will be addressed
501 in future work.

502 *c. 2D (x-z) squall line*

503 We perform a test case of a 2D squall line as described in Weisman and Klemp (1982)
 504 to evaluate mass conservation, consistency, and shape-preservation in the nonhydrostatic
 505 solver, in addition to testing for any small-scale computational instability in the model due
 506 to latent heating.

507 The numerical domain is centered at $x = 0.0$ km, with $-100 \text{ km} \leq x \leq 100 \text{ km}$ and
 508 $0 \leq z \leq 20 \text{ km}$. As in Weisman and Klemp (1982), a conditionally unstable thermodynamic
 509 profile is used to initialize the horizontally homogeneous environment. Constant physical
 510 horizontal and vertical eddy viscosities of $250 \text{ m}^2 \text{ s}^{-1}$ are used. A warm thermal perturbation
 511 near the surface is prescribed to initiate convection (Weisman et al. 1988). The initial thermal
 512 perturbation has a maximum of $\Delta\theta_0 = 3 \text{ K}$, centered at $z_c = 1.5 \text{ km}$ and along the centerline
 513 ($x_c = 0$) of the domain, with a horizontal radius x_r of 10 km and a vertical radius z_r of 1.5
 514 km. The shape of the perturbation is a cosine hill given as

$$\theta(x, z, t = 0) = \begin{cases} \Delta\theta_0 \cos^2(\pi L/2) & , L < 1.0, \\ 0 & , L \geq 1.0, \end{cases}$$

515 where $L = \sqrt{(x/x_r)^2 + [(z - z_c)/z_r]^2}$.

516 A weak vertical wind shear within a 2.5 km -layer at the surface is used to promote the
 517 growth of the squall line. The initial wind profile is given as

$$u(z, t = 0) = \begin{cases} \bar{u} \cdot (z/z_{ts}) - u_s & , z < z_{ts}, \\ \bar{u} - u_s & , z \geq z_{ts}, \end{cases}$$

518 where $\bar{u} = 12 \text{ m s}^{-1}$, $u_s = 10 \text{ m s}^{-1}$, and $z_{ts} = 2.5 \text{ km}$. The environmental potential
 519 temperature and relative humidity profiles at the initial time are

$$\bar{\theta}(z, t = 0) = \begin{cases} \theta_0 + (\theta_{tr} - \theta_0)(z/z_{tr})^{\frac{5}{4}} & , z \leq z_{tr}, \\ \theta_{tr} \exp \left[\frac{g}{c_p T_{tr}} (z - z_{tr}) \right] & , z > z_{tr}, \end{cases}$$

520 and

$$RH(z, t = 0) = \begin{cases} 1 - \frac{3}{4}(z/z_{tr})^{\frac{5}{4}} & , z \leq z_{tr}, \\ 0.25 & , z > z_{tr}, \end{cases}$$

521 where $\theta_{tr} = 343$ K, $z_{tr} = 12.0$ km, and $T_{tr} = 213$ K are the potential temperature, geometric
522 height, and actual temperature at the tropopause. The maximum water mixing ratio is
523 capped at 14 g kg^{-1} . The surface potential temperature $\theta_0 = 300$ K. The skew- T log- p
524 diagram for this sounding can be found in Fig. 1 of Weisman and Klemp (1982). Numerical
525 simulations (unless otherwise stated) use a grid spacing $\Delta x = \Delta z = 500$ m, a time step
526 $\Delta t = 5$ s, and a time-off-centering parameter of $\beta = 0.1$ to maintain numerical stability.
527 Like the gravity case, the boundary condition is implemented by linear extrapolating u , Θ ,
528 and ρ values into the boundary and setting $w = 0$, consistent with the free-slip boundary
529 conditions.

530 A comparison of the squall line development among CSLAM-NH (with shape preserva-
531 tion), the 5th-order split-explicit, and the 2nd-order split-explicit Eulerian models is pre-
532 sented in Fig. 8. Instantaneous and accumulated surface precipitation integrated across the
533 model domain are presented in Fig. 9; also shown is the rate of condensation over the entire
534 domain. Maximum updraft velocity is shown in Fig. 10. The series of updraft velocity peaks
535 highlight the continuous triggering of new convective systems along the advancing front.

536 All three models (CSLAM-NH, Eulerian 5th-order advection, and Eulerian 2nd-order
537 advection) show similar development of the convective system (Fig. 8). At 0.6 h, all three
538 models show an initial downshear orientation of the system due to the ambient wind shear.
539 As the storm continues to develop with the cold pool strengthening behind the system (not
540 shown), convergence and enhanced uplift lead to the storm tilting in a near-upright position
541 ($T = 0.8$ h). At 1.3 h, a new cell is triggered near the edge of the cold pool, where uplift
542 of the warm moist air in the boundary layer is enhanced. At 1.7 h, the cold pool is strong
543 enough to generate a circulation such that the system develops an upshear orientation, as
544 described in Rotunno et al. (1988). Comparing to the simulations from the Eulerian 2nd-

545 order model, those from CSLAM-NH show closer resemblance to those from the Eulerian
546 5th-order model. The better agreement is also evident in the moisture statistics (Fig. 9),
547 especially in the accumulated surface precipitation amounts and condensation rate in the
548 domain.

549 Focussing on the two models that show more comparable results, the first maximum
550 updraft velocities from CSLAM-NH (34.1 m s^{-1}) is slightly greater than that from Eulerian
551 5th-order advection (31.6 m s^{-1}) (Fig. 10). CSLAM-NH appears to show a weaker second
552 peak updraft velocity (21.9 m s^{-1}) than the Eulerian 5th-order model (28.3 m s^{-1}); however,
553 the stronger first peak ($\sim 34 \text{ m s}^{-1}$) and weaker second peak ($\sim 25 \text{ m s}^{-1}$) are also observed
554 in a higher-resolution simulation using the Eulerian 5th-order model at a grid spacing of 250
555 m and large time step size of 2.5 s (dashed black line in Fig. 10). For comparison, maximum
556 updraft from CSLAM-NH at $\Delta x = 250 \text{ m}$ and $\Delta t = 2.5 \text{ s}$ (red dashed line in Fig. 10) is also
557 shown, and at the higher resolution, the two models agree very well with each other.

558 The maximum stable time step in the Eulerian split-explicit 5th-order advection scheme
559 is a large time step of 20 s and acoustic time step size of 1.25 s. The maximum CSLAM-NH
560 stable time step is limited to 15 s due to the violation of the Lipschitz stability condition in
561 the vicinity of the updraft when a larger time step is used (the instability occurs when the
562 storm reaches its first maximum vertical updraft, which generates a strong horizontal wind
563 shear between the updraft and the neighbouring downdraft). In Fig. 11, we see at larger
564 time step sizes, maximum updraft velocities remain close to the small time-step solutions.

565 With the 2D squall-line test case, we examine the shape-preservation properties of CSLAM-
566 NH using the shape-preserving scheme by Barth and Jespersen (1989) in the CSLAM trans-
567 port scheme and the upwind scheme for the flux-correction terms in the transport equations.
568 An analogous implementation of these schemes for a shallow-water model is described in
569 Wong et al. (2013).

570 To verify that consistency is achieved, an additional passive tracer with mixing ratio r is
571 introduced into the model. The passive tracer initially has a constant mixing ratio of $r_0 =$

572 1.0 g kg⁻¹ and we form the discretized conservation equation as in (23). The minimum and
573 maximum values of r are maintained at 1.0 g kg⁻¹ (up to machine roundoff of order 10⁻¹⁴)
574 throughout the simulation using the consistent formulation in CSLAM-NH.

575 For a passive tracer that uses an inconsistent discrete conservation equation such as (26),
576 unphysical minima and maxima of the passive tracer mixing ratio are generated (Fig. 12).
577 At the end of the squall line simulation at 2 h, the minimum and maximum mixing ratios
578 r are 0.986 g kg⁻¹ and 1.021 g kg⁻¹, respectively (i.e. the error is on the order of 1 part in
579 100). We note that the shape-preserving limiter described in Barth and Jespersen (1989)
580 was also applied in CSLAM in this test. Due to numerical inconsistency, however, the limiter
581 becomes ineffective agreeing with the results in Wong et al. (2013). This discrepancy from
582 constancy highlights the importance of ensuring numerical consistency to properly maintain
583 conservation of moisture and tracer mass in a semi-implicit CISK solver.

584 6. Summary

585 A new cell-integrated semi-Lagrangian (CISK) nonhydrostatic atmospheric solver, CSLAM-
586 NH, for the moist Euler equations is introduced in this paper. The two-dimensional (x - z)
587 Cartesian nonhydrostatic solver uses a CISK transport scheme, CSLAM, for conservative
588 transport. It also incorporates a new approach to ensure numerical consistency among the
589 CISK continuity equation and the conservation equations for potential temperature, mois-
590 ture species, and passive tracers. A semi-implicit time integration scheme is used to stably
591 handle the fast-moving acoustic waves in the compressible system.

592 Based on a recently tested shallow-water equations solver, the extended nonhydrostatic
593 atmospheric solver presented here, CSLAM-NH, possesses a number of features ideal for
594 weather and climate modelling purposes. The solver:

- 595 i. is inherently mass-conserving through the use of a conservative transport scheme
596 CSLAM,

- 597 ii. ensures numerical consistency between the continuity equation and other scalar mass
598 conservation equations (the lack of which may lead to violation of scalar mass conser-
599 vation),
- 600 iii. does not depend on a mean reference state,
- 601 iv. can be easily implemented with existing shape-preserving filters to ensure shape-
602 preservation of scalar fields,
- 603 v. requires a single linear Helmholtz equation solution (as in typical semi-implicit solvers)
604 per time step, and
- 605 vi. requires a single application of CSLAM per time step.

606 Here, we tested the nonhydrostatic extension for three idealized test cases: a density
607 current, a gravity wave, and a squall line. To represent microphysical processes in the squall
608 line test, the Kessler warm-rain microphysics parameterization scheme is coupled to the
609 dynamics. The 2D solver currently does not admit flow in the y -direction, and therefore,
610 Coriolis terms are neglected; however, the tests we present allow for sufficient testing of
611 typical meteorological flows. Results compare well with other existing Eulerian (such as
612 WRF-ARW) and nonhydrostatic CISL solvers (such as the nonhydrostatic SLICE model).
613 In the density current and gravity wave tests, we see that CSLAM-NH allows for stable time
614 steps two times larger than that in an Eulerian model. In the highly-nonhydrostatic flow
615 of the squall line test case, the maximum stable time step size is of similar magnitude as
616 the Eulerian split-explicit model. The strong wind shear across the storm updraft imposes
617 a time step limit in CSLAM-NH due to the Lipschitz stability condition (violation of which
618 leads to the crossing of trajectories).

619 Plans to extend the nonhydrostatic solver to include orographic influences are also un-
620 derway. This work involves transformation of the nonhydrostatic equations into a terrain-
621 following height coordinate. In traditional semi-Lagrangian semi-implicit solvers, flow over

622 topography has been found to trigger spurious resonances and time off-centering in the im-
623 plicit scheme has been found to eliminate these noises. Thus far, without orography, we have
624 found that our nonhydrostatic solver only requires time off-centering ($\beta = 0.1$) in the squall
625 line case to maintain numerical stability. The nonhydrostatic solver with orography will al-
626 low us to test the conservative and consistent transport and stability of the new semi-implicit
627 CISL discretization under the influence of a terrain-following coordinate.

628 *Acknowledgments.*

629 This work was done as a part of the National Center for Atmospheric Research - Graduate
630 Visitor Advanced Study Program. The first author would also like to acknowledge the
631 Canadian Natural Science and Engineering Research Council for their financial support via
632 the Discovery Grant to the last author.

633

REFERENCES

634

635 Barth, T. J. and D. C. Jespersen, 1989: The design and application of upwind schemes on
636 unstructured meshes. *27th Aerospace Sciences Meeting*, **89 (89-0366)**.

637 Erath, C., P. H. Lauritzen, J. H. Garcia, and H. M. Tufo, 2012: Integrating a scalable and
638 efficient semi-Lagrangian multi-tracer transport scheme in HOMME. *Procedia Computer
639 Science*, **9**, 994–1003.

640 Erath, C., P. H. Lauritzen, and H. M. Tufo, 2013: On mass-conservation in high-order high-
641 resolution rigorous remapping schemes on the sphere. *Mon. Wea. Rev.*, **141**, 2128–2133.

642 Harris, L. M., P. H. Lauritzen, and R. Mittal, 2011: A flux-form version of the conservative
643 semi-Lagrangian multi-tracer transport scheme (CSLAM) on the cubed sphere grid. *J.
644 Comput. Phys.*, **230**, 1215–1237.

645 Jablonowski, C., 2004: Adaptive grids in weather and climate modeling. Ph.D. thesis, Uni-
646 versity of Michigan, 292 pp.

647 Jöckel, P., R. von Kuhlmann, M. Lawrence, B. Steil, C. Brenninkmeijer, P. Crutzen,
648 P. Rasch, and B. Eaton, 2001: On a fundamental problem in implementing flux-form
649 advection schemes for tracer transport in 3-dimensional general circulation and chemistry
650 transport models. *Q. J. R. Meteorol. Soc.*, **127**, 1035–1052.

651 Klemp, J. B., W. C. Skamarock, and J. Dudhia, 2007: Conservative split-explicit time
652 integration methods for the compressible nonhydrostatic equations. *Mon. Wea. Rev.*, **135**,
653 2897–2913.

654 Klemp, J. B. and R. B. Wilhelmson, 1978: The Simulation of Three-Dimensional Convective
655 Storm Dynamics. *J. Atmos. Sci.*, **35**, 1070–1096.

- 656 Laprise, J. and A. Plante, 1995: A class of semi-Lagrangian integrated-mass (SLIM) numer-
657 ical transport algorithms. *Mon. Wea. Rev.*, **123**, 553–565.
- 658 Lauritzen, P. H., E. Kaas, and B. Machenhauer, 2006: A mass-conservative semi-implicit
659 semi-Lagrangian limited-area shallow-water model on the sphere. *Mon. Wea. Rev.*, **134**,
660 1205–1221.
- 661 Lauritzen, P. H., E. Kaas, B. Machenhauer, and K. Lindberg, 2008: A mass-conservative
662 version of the semi-implicit semi-Lagrangian HIRLAM. *Q. J. R. Meteorol. Soc.*, **134**,
663 1583–1595.
- 664 Lauritzen, P. H., R. D. Nair, and P. A. Ullrich, 2010: A conservative semi-Lagrangian multi-
665 tracer transport scheme (CSLAM) on the cubed-sphere grid. *J. Comput. Phys.*, **229**,
666 1401–1424.
- 667 Lauritzen, P. H., W. C. Skamarock, M. J. Prather, and M. A. Taylor, 2012: A standard
668 test case suite for two-dimensional linear transport on the sphere. *Geosci. Model Dev.*, **5**,
669 887–901.
- 670 Lauritzen, P. H., et al., 2013: A standard test case suite for two-dimensional linear transport
671 on the sphere: results from a collection of state-of-the-art schemes. *Geosci. Model Dev.*
672 *Discuss.*, **6 (3)**, 4983–5076.
- 673 Machenhauer, B., E. Kaas, and P. H. Lauritzen, 2009: Finite volume meteorology. *Com-*
674 *putational Methods for the Atmosphere and the Oceans: Special Volume*, R. Temam and
675 J. Tribbia, Eds., Elsevier, *Handb. Numer. Anal.*, 3–120.
- 676 Machenhauer, B. and M. Olk, 1997: The implementation of the semi-implicit scheme in
677 cell-integrated semi-Lagrangian models. *Atmos.-Ocean*, **35 (special issue)**, 103–126.
- 678 McGregor, J. L., 1993: Economical determination of departure points for semi-Lagrangian
679 models. *Mon. Wea. Rev.*, **121**, 221–230.

- 680 Melvin, T., M. Dubal, N. Wood, A. Staniforth, and M. Zerroukat, 2010: An inherently mass-
681 conserving iterative semi-implicit semi-Lagrangian discretization of the non-hydrostatic
682 vertical-slice equations. *Q. J. R. Meteorol. Soc.*, **136**, 799–814.
- 683 Nair, R. and B. Machenhauer, 2002: The mass-conservative cell-integrated semi-Lagrangian
684 advection scheme on the sphere. *Mon. Wea. Rev.*, **130**, 649–667.
- 685 Nair, R. D. and P. H. Lauritzen, 2010: A class of deformational flow test cases for linear
686 transport problems on the sphere. *J. Comput. Phys.*, **229**, 8868–8887.
- 687 Rancic, M., 1992: Semi-Lagrangian piecewise biparabolic scheme for two-dimensional hori-
688 zontal advection of a passive scalar. *Mon. Wea. Rev.*, **120**, 1394–1406.
- 689 Rasch, P. and D. Williamson, 1990: Computational aspects of moisture transport in global-
690 models of the atmosphere. *Q. J. R. Meteorol. Soc.*, **116**, 1071–1090.
- 691 Robert, A., 1981: A stable numerical integration scheme for the primitive meteorological
692 equations. *Atmos.-Ocean*, **19**, 35–46.
- 693 Robert, A., T. Yee, and H. Ritchie, 1985: A semi-Lagrangian and semi-implicit numerical-
694 integration scheme for multilevel atmospheric models. *Mon. Wea. Rev.*, **113**, 388–394.
- 695 Rotunno, R., J. B. Klemp, and M. L. Weisman, 1988: A theory for strong, long-lived squall
696 lines. *J. Atmos. Sci.*, **45**, 463–485.
- 697 Skamarock, W. C. and J. B. Klemp, 1994: Efficiency and accuracy of the Klemp-Wilhelmson
698 time-splitting technique. *Mon. Wea. Rev.*, **122**, 2623–2630.
- 699 Skamarock, W. C. and J. B. Klemp, 2008: A time-split nonhydrostatic atmospheric model
700 for weather research and forecasting applications. *J. Comput. Phys.*, **227**, 3465–3485.
- 701 Straka, J., R. B. Wilhelmson, L. J. Wicker, J. R. Anderson, and K. K. Droegemeier, 1992:
702 Numerical solutions of a non-linear density current: A benchmark solution and compar-
703 isons. *Int. J. Numer. Methods Fluids*, **17**, 1–22.

- 704 Ullrich, P. A., P. H. Lauritzen, and C. Jablonowski, 2012: Some considerations for high-order
705 ‘incremental remap’-based transport schemes: edges, reconstructions, and area integra-
706 tion. *Int. J. Numer. Methods Fluids*, **71**, 1131–1151.
- 707 Weisman, M. L. and J. B. Klemp, 1982: The dependence of numerically simulated convective
708 storms on vertical wind shear and buoyancy. *Mon. Wea. Rev.*, **110**, 504–520.
- 709 Weisman, M. L., J. B. Klemp, and R. Rotunno, 1988: Structure and evolution of numerically
710 simulated squall lines. *J. Atmos. Sci.*, **45**, 1990–2013.
- 711 Wong, M., W. C. Skamarock, P. H. Lauritzen, and R. B. Stull, 2013: A cell-integrated
712 semi-Lagrangian semi-implicit shallow-water model (CSLAM-SW) with conservative and
713 consistent transport. *Mon. Wea. Rev.*, **141**, 2545–2560.
- 714 Xue, M., K. K. Droegemeier, and V. Wong, 2000: The Advanced Regional Prediction System
715 (ARPS) - A multi-scale nonhydrostatic atmospheric simulation and prediction model. Part
716 I: Model dynamics and verification. *Meteorol. Atmos. Phys.*, **75**, 161–193.
- 717 Zerroukat, M., N. Wood, and A. Staniforth, 2002: SLICE: A semi-Lagrangian inherently
718 conserving and efficient scheme for transport problems. *Q. J. R. Meteorol. Soc.*, **128**,
719 2801–2820.
- 720 Zhang, K., H. Wan, B. Wang, and M. Zhang, 2008: Consistency problem with tracer advec-
721 tion in the atmospheric model GAMIL. *Adv. Atmos. Sci.*, **25**, 306–318.

722 List of Tables

- 723 1 Statistics for the density current simulations at time 15 min using CSLAM-
724 NH at various grid resolutions and time step sizes. Comparison values from
725 the nonhydrostatic x - z solver using SLICE in Melvin et al. (2010) are also
726 presented. REFC25 are values taken from Straka et al. (1992). θ'_{sampled} are
727 solutions sampled at 200 m for comparison with values in Straka et al. (1992). 35

Grid size (m)	Time step size (s)	θ'_{\min} (K)	θ'_{\max} (K)	Front location (m)	$\sum \theta'_{\text{sampled}}$ (K)	$\sum \theta'_{\text{sampled}}$ (for $\theta' > 0$) (K)	$\sum \theta'^2_{\text{sampled}}$ (K ²)
400	4	-10.339	0.6804	14248	—	—	—
200	2	-10.746	0.0846	14938	-1293.82	4.4398×10^{-1}	5634.92
100	1	-9.7694	0.0006	15234	-1361.41	1.8114×10^{-4}	6127.90
100	4	-9.6985	0.0053	15256	-1360.73	6.7741×10^{-3}	6182.03
50	0.5	-9.7078	0.0000	15360	-1394.93	2.0562×10^{-5}	6395.63
25	0.25	-9.7323	0.0000	15391	-1411.62	3.2974×10^{-8}	6516.33
SLICE400	4	-5.6608	0.3674	13572	—	—	—
SLICE200	2	-8.0958	0.1226	14768	—	—	—
SLICE100	1	-9.8574	0.0995	15182	—	—	—
SLICE50	0.5	-9.4995	0.0626	15334	—	—	—
SLICE25	0.25	-9.6548	0.0048	15390	—	—	—
REFC25	1.5625×10^{-2}	-9.7738	0.0000	15537	-1427.10	0.0000	6613.62

TABLE 1. Statistics for the density current simulations at time 15 min using CSLAM-NH at various grid resolutions and time step sizes. Comparison values from the nonhydrostatic x - z solver using SLICE in Melvin et al. (2010) are also presented. REFC25 are values taken from Straka et al. (1992). θ'_{sampled} are solutions sampled at 200 m for comparison with values in Straka et al. (1992).

List of Figures

- 728
- 729 1 (a) Exact departure cell area (δA^* , dark grey region) and the corresponding
730 arrival grid cell (ΔA , light grey region). (b) Departure cells in CSLAM (δA)
731 are represented as polygons defined by the departure locations of the arrival
732 grid cell vertices. (Wong et al. 2013) 38
- 733 2 Geometric representation of the Lagrangian flux divergence, defined as the
734 flux-area difference between the Eulerian arrival grid cell (solid square) and
735 the departure cell (dashed polygon) in one time step. Velocities associated
736 with the Eulerian grid cell at the cell faces (u_l, u_r, w_t, w_b) and cell vertices
737 (u_c, w_c)_{*i*} for $i = 1, 2, 3, 4$ are also shown. White arrows indicate the computed
738 trajectories of each departure grid cell vertex. 39
- 739 3 Potential temperature perturbation (K) after 15 min. Contour intervals are
740 every 1 K, starting at 0.5 K. Mean wind $\bar{U} = 0 \text{ m s}^{-1}$. 40
- 741 4 Potential temperature perturbation (K) after 15 min. Contoured as in Fig.
742 3. Solution is translated using a mean wind $\bar{U} = 20 \text{ m s}^{-1}$. 41
- 743 5 Potential temperature perturbation (K) from CSLAM-NH after 15 min for
744 grid spacing $\Delta x = \Delta z = 100 \text{ m}$ using time step sizes $\Delta t = 3$ and 4 s . Mean
745 wind $\bar{U} = 0 \text{ m s}^{-1}$. The Eulerian split-explicit scheme (not plotted) was
746 numerically unstable for these time steps, as it required $\Delta t \leq 2 \text{ s}$ for numerical
747 stability of this gravity current. Contoured as in Fig. 3. 42
- 748 6 Potential temperature perturbation (K) after 50 min. Contour intervals are
749 every $5 \times 10^{-4} \text{ K}$ (zero contour line not plotted). Solid lines indicate positive
750 contours and dashed lines indicate negative contours. Solution is translated
751 using a mean wind $\bar{U} = 20 \text{ m s}^{-1}$. Horizontal axis has also been translated
752 with the mean wind so the line of symmetry remains at $x = 0$. 43

- 753 7 Potential temperature perturbation (K) solutions of the gravity wave case
754 using increasingly large CSLAM-NH time steps ($\Delta x = \Delta z = 1$ km) where
755 (a)-(c) $\bar{U} = 0$ m s⁻¹ and (d)-(f) $\bar{U} = 20$ m s⁻¹. Contoured as in Fig. 6. 44
- 756 8 Vertical cross-sections of vertical velocity (color shading in m s⁻¹) and solid
757 contour of the convective cloud structure ($q_c = 0.1$ g kg⁻¹) at times 0.6, 0.8,
758 1.3, 1.7 h of the simulation for the 500 m grid-spacing runs with a time step of
759 5.0 s from (left) CSLAM-NH, (middle) 5th-order split-explicit Eulerian model,
760 and (right) 2nd-order split-explicit Eulerian model. 45
- 761 9 Moisture statistics including surface precipitation rate (kg s⁻¹), accumulated
762 surface precipitation (kg), and condensation rate (kg s⁻¹) from the micro-
763 physics using CSLAM-NH, Eulerian 5th-order horizontal advection, and Eu-
764 lerian 2nd-order horizontal advection at $\Delta x = \Delta z = 500$ m. 46
- 765 10 Updraft intensities using CSLAM-NH (red) and Eulerian 5th-order horizontal
766 advection (black) at $\Delta x = \Delta z = 500$ m and $\Delta t = 5$ s (solid), and $\Delta x = \Delta z =$
767 250 m and $\Delta t = 2.5$ s (dashed). 47
- 768 11 Timing and intensity of the maximum vertical updraft using $\Delta x = \Delta z = 500$
769 m at different CSLAM-NH time step sizes (solid lines), as compared to the
770 Eulerian 5th-order horizontal advection vertical velocity (dashed lines). (Only
771 first hour is plotted.) 48
- 772 12 Mixing ratio errors (g kg⁻¹) due to numerical inconsistency associated with
773 (26). The passive tracer is initialized with a uniform mixing ratio field of
774 1.0 g kg⁻¹. The consistent formulation in CSLAM-NH (which does not use
775 (26)) ensures mixing ratio constancy of the same passive tracer up to machine
776 roundoff of order 10^{-14} (not shown). 49

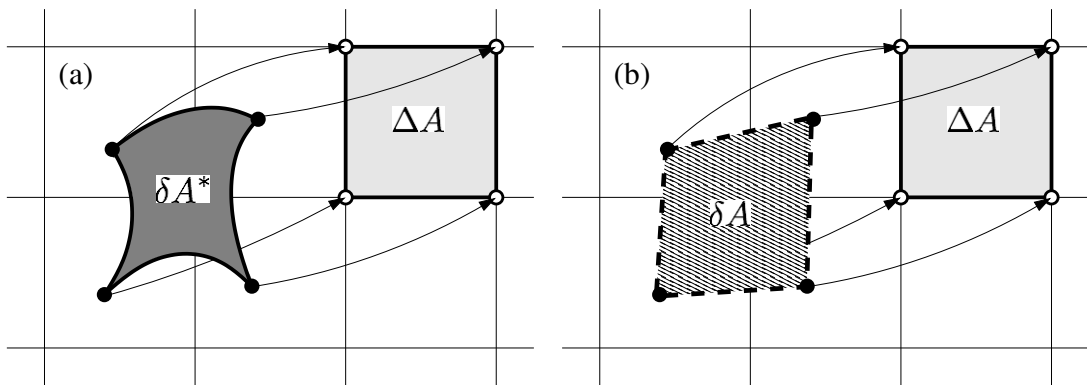


FIG. 1. (a) Exact departure cell area (δA^* , dark grey region) and the corresponding arrival grid cell (ΔA , light grey region). (b) Departure cells in CSLAM (δA) are represented as polygons defined by the departure locations of the arrival grid cell vertices. (Wong et al. 2013)

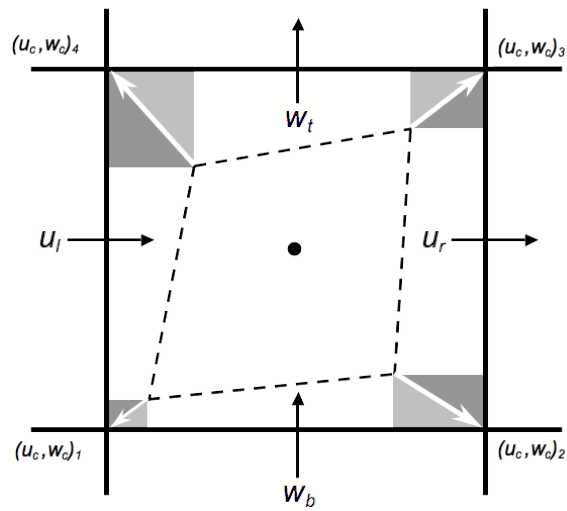


FIG. 2. Geometric representation of the Lagrangian flux divergence, defined as the flux-area difference between the Eulerian arrival grid cell (solid square) and the departure cell (dashed polygon) in one time step. Velocities associated with the Eulerian grid cell at the cell faces (u_l, u_r, w_t, w_b) and cell vertices $(u_c, w_c)_i$ for $i = 1, 2, 3, 4$ are also shown. White arrows indicate the computed trajectories of each departure grid cell vertex.

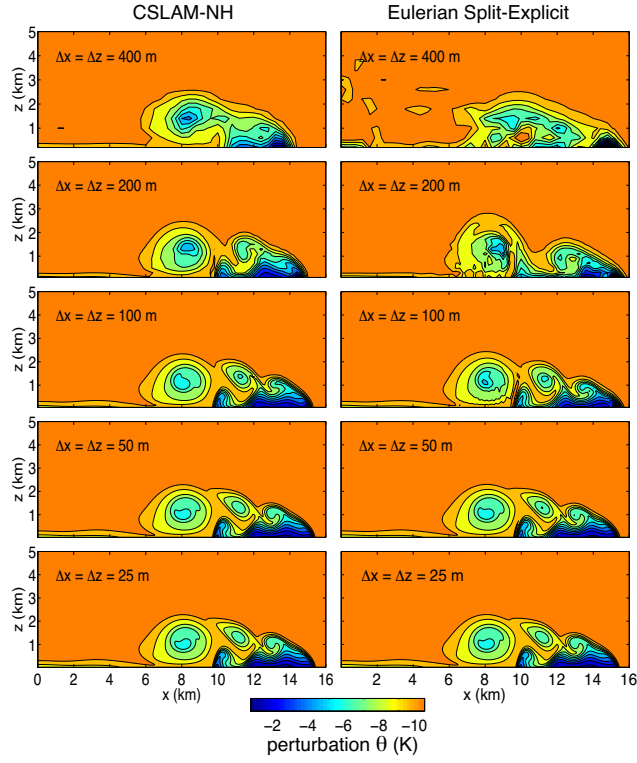


FIG. 3. Potential temperature perturbation (K) after 15 min. Contour intervals are every 1 K, starting at 0.5 K. Mean wind $\bar{U} = 0 \text{ m s}^{-1}$.

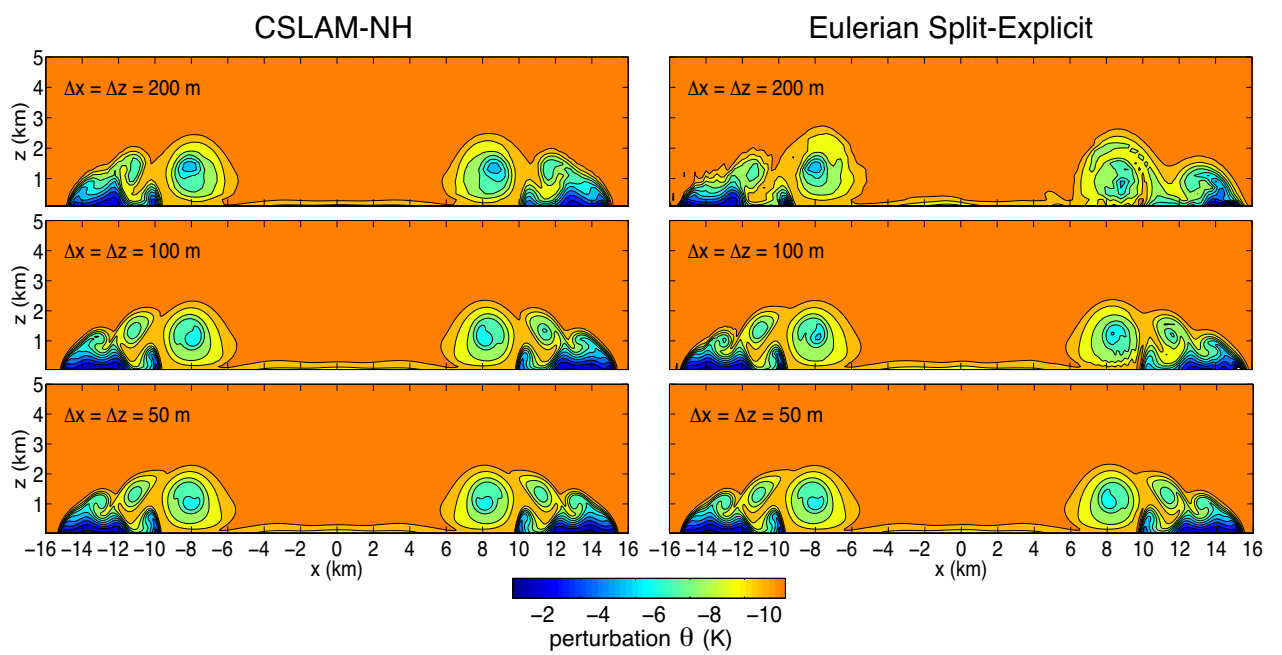


FIG. 4. Potential temperature perturbation (K) after 15 min. Contoured as in Fig. 3. Solution is translated using a mean wind $\bar{U} = 20 \text{ m s}^{-1}$.

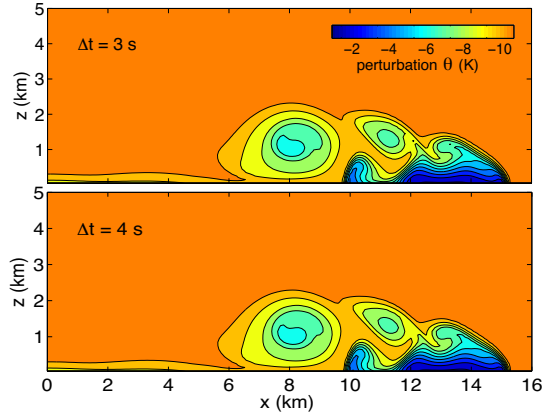


FIG. 5. Potential temperature perturbation (K) from CSLAM-NH after 15 min for grid spacing $\Delta x = \Delta z = 100$ m using time step sizes $\Delta t = 3$ and 4 s. Mean wind $\bar{U} = 0$ m s^{-1} . The Eulerian split-explicit scheme (not plotted) was numerically unstable for these time steps, as it required $\Delta t \leq 2$ s for numerical stability of this gravity current. Contoured as in Fig. 3.

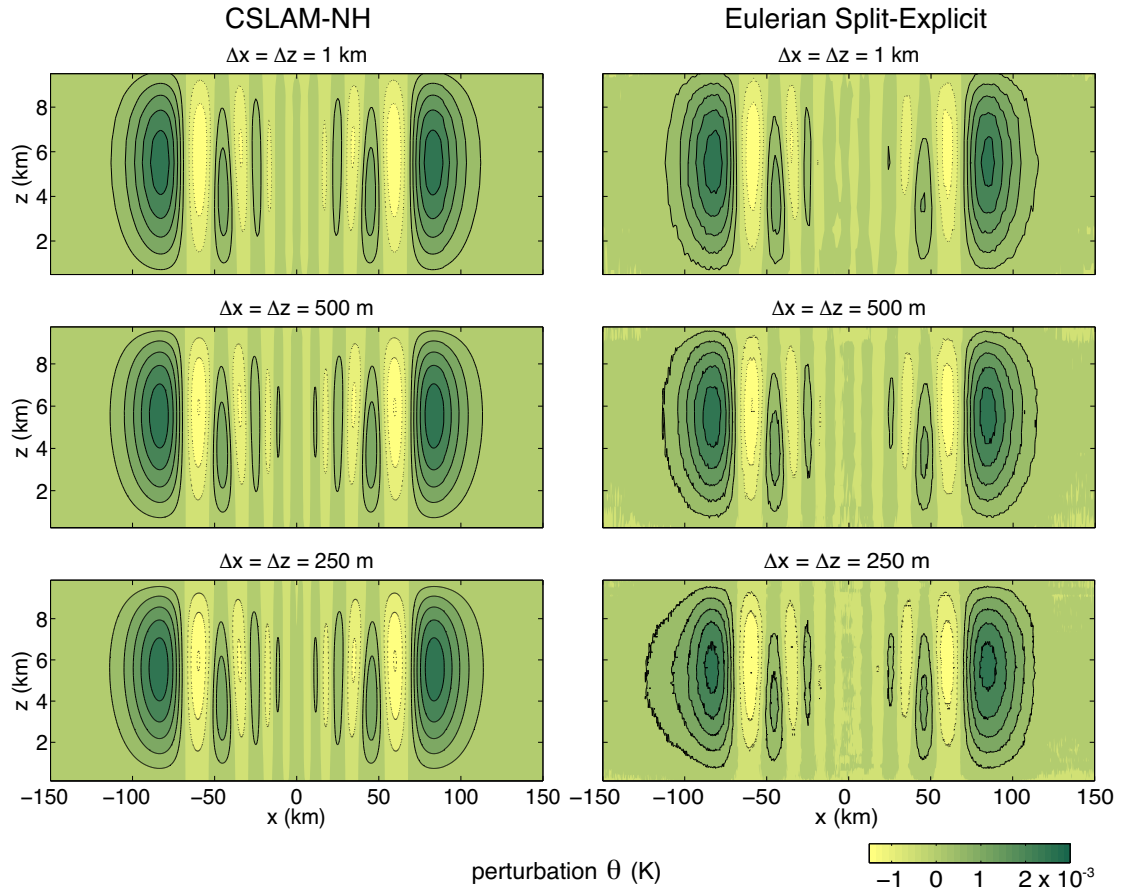


FIG. 6. Potential temperature perturbation (K) after 50 min. Contour intervals are every 5×10^{-4} K (zero contour line not plotted). Solid lines indicate positive contours and dashed lines indicate negative contours. Solution is translated using a mean wind $\bar{U} = 20 \text{ m s}^{-1}$. Horizontal axis has also been translated with the mean wind so the line of symmetry remains at $x = 0$.

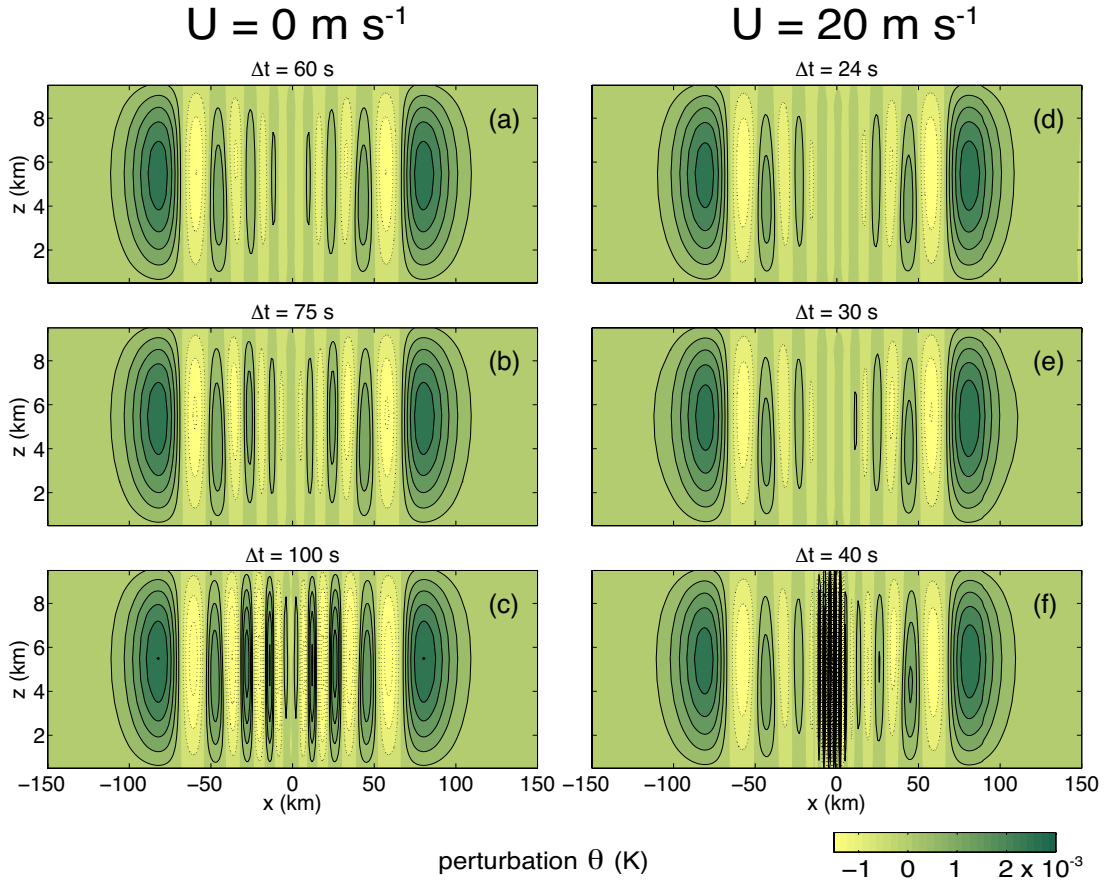


FIG. 7. Potential temperature perturbation (K) solutions of the gravity wave case using increasingly large CSLAM-NH time steps ($\Delta x = \Delta z = 1 \text{ km}$) where (a)-(c) $\bar{U} = 0 \text{ m s}^{-1}$ and (d)-(f) $\bar{U} = 20 \text{ m s}^{-1}$. Contoured as in Fig. 6.

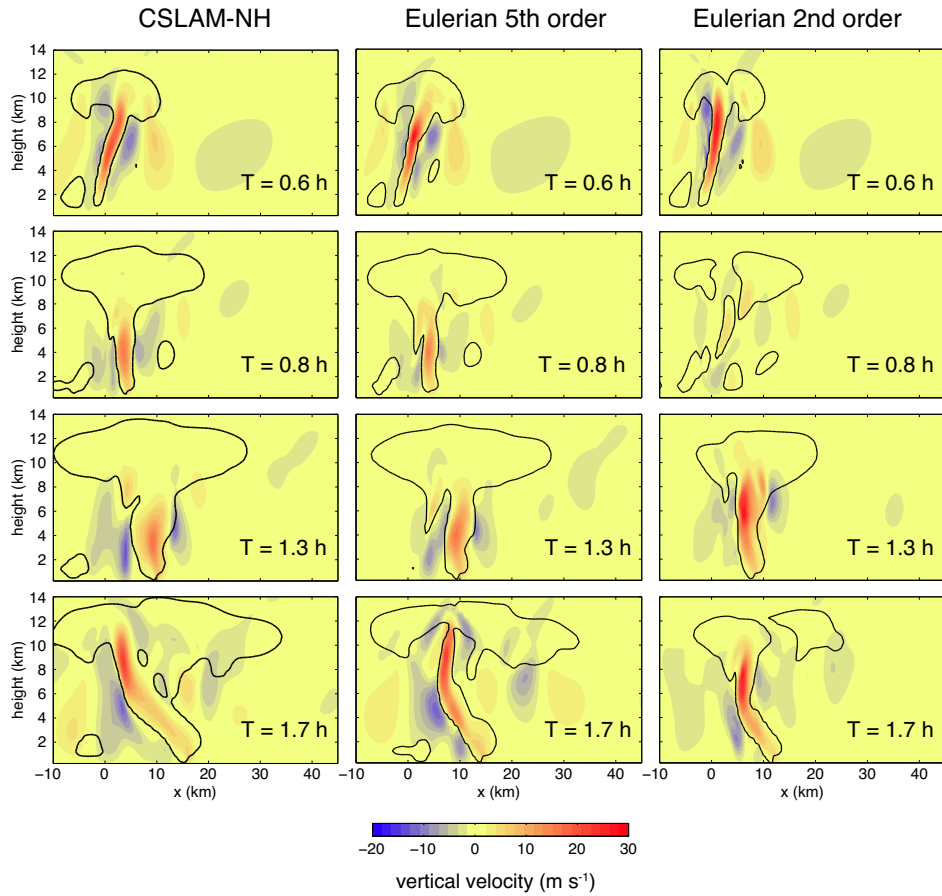


FIG. 8. Vertical cross-sections of vertical velocity (color shading in m s^{-1}) and solid contour of the convective cloud structure ($q_c = 0.1 \text{ g kg}^{-1}$) at times 0.6, 0.8, 1.3, 1.7 h of the simulation for the 500 m grid-spacing runs with a time step of 5.0 s from (left) CSLAM-NH, (middle) 5th-order split-explicit Eulerian model, and (right) 2nd-order split-explicit Eulerian model.

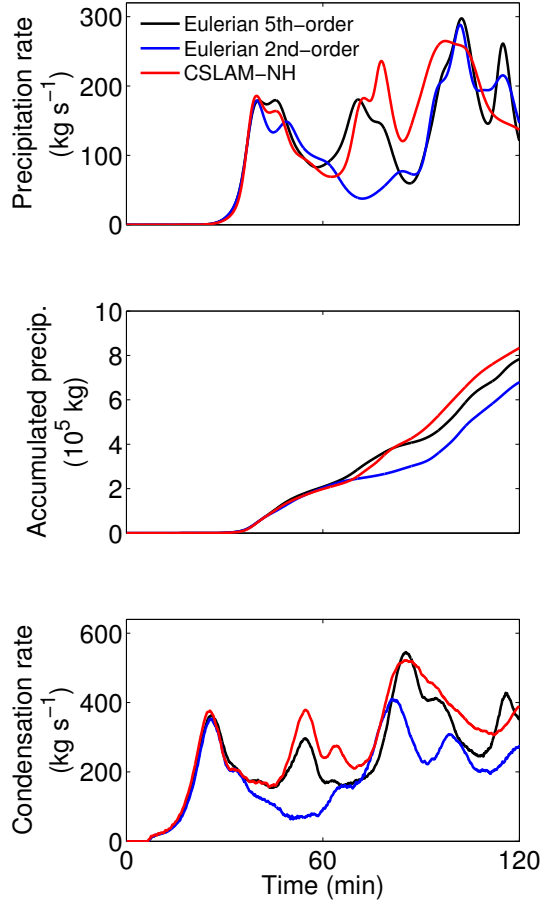


FIG. 9. Moisture statistics including surface precipitation rate (kg s^{-1}), accumulated surface precipitation (kg), and condensation rate (kg s^{-1}) from the microphysics using CSLAM-NH, Eulerian 5th-order horizontal advection, and Eulerian 2nd-order horizontal advection at $\Delta x = \Delta z = 500$ m.

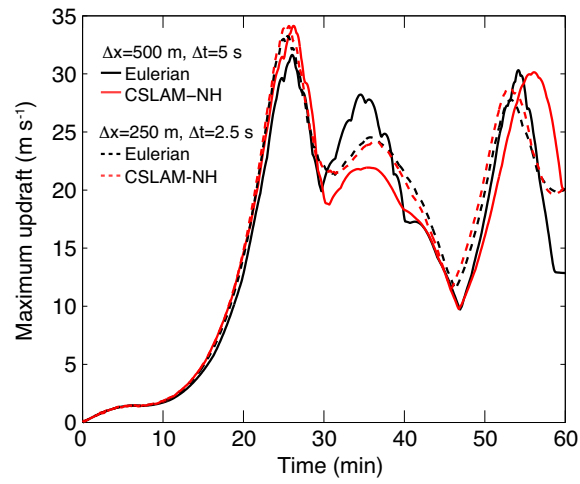


FIG. 10. Updraft intensities using CSLAM-NH (red) and Eulerian 5th-order horizontal advection (black) at $\Delta x = \Delta z = 500$ m and $\Delta t = 5$ s (solid), and $\Delta x = \Delta z = 250$ m and $\Delta t = 2.5$ s (dashed).

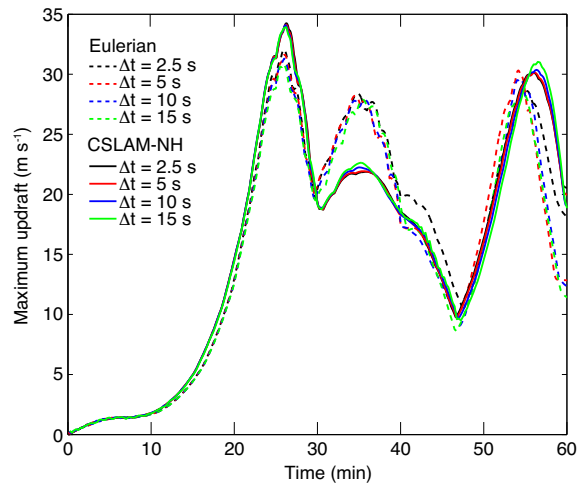


FIG. 11. Timing and intensity of the maximum vertical updraft using $\Delta x = \Delta z = 500$ m at different CSLAM-NH time step sizes (solid lines), as compared to the Eulerian 5th-order horizontal advection vertical velocity (dashed lines). (Only first hour is plotted.)

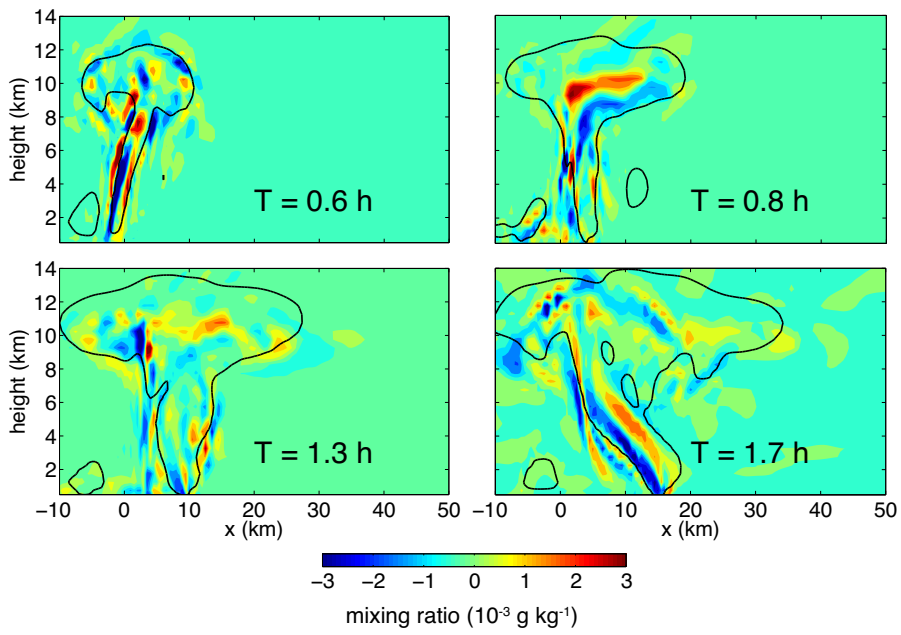


FIG. 12. Mixing ratio errors (g kg^{-1}) due to numerical inconsistency associated with (26). The passive tracer is initialized with a uniform mixing ratio field of 1.0 g kg^{-1} . The consistent formulation in CSLAM-NH (which does not use (26)) ensures mixing ratio constancy of the same passive tracer up to machine roundoff of order 10^{-14} (not shown).